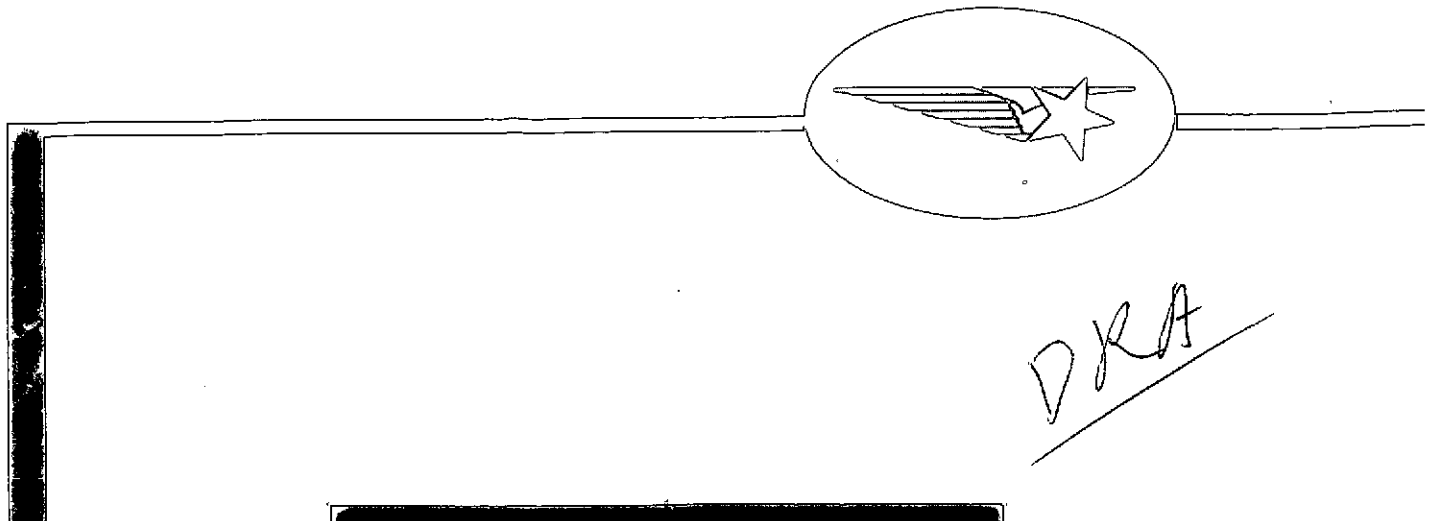

DRA

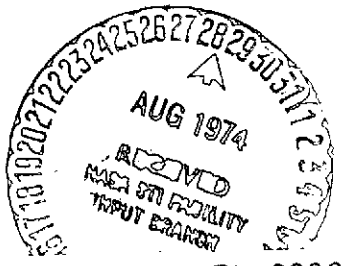

(NASA-CR-120376) THE SPECTRA SPECTROHELIOGRAPH SYSTEM, SECTION 1 Final Report (Lockheed Missiles and Space Co.) 61 p HC $6.25 CSCL 14B

N74-30891

Unclas
G3/14 17091

58

Lockheed

MISSILES & SPACE COMPANY, INC.
A SUBSIDIARY OF LOCKHEED AIRCRAFT CORPORATION
SUNNYVALE, CA

58

FINAL REPORT

Section I

THE SPECTRA SPECTROHELIOGRAPH SYSTEM

May 1974

Prepared for

George C. Marshall Space Flight Center
Huntsville, Alabama 35812

Contract No. NAS8-28018

Principal Investigator: Dr. A. M. Title

Lockheed Solar Observatory
Lockheed Palo Alto Research Laboratory
3251 Hanover Street
Palo Alto, California 94304

TABLE OF CONTENTS

A. SUMMARY

The basic objective of the contract was to create a system capable of producing maps of the magnetic field straight from spectra. The theory of the extraction of magnetic field information is contained in Section I in Part B on measurement of the magnetic field by fourier transform techniques. Part C contains contour maps of a high gradient magnetic field region. Section II is an operators manual, program description, and the Fortran coding for the implementation of the measurement procedures. Section III is an operators manual for microdensitometer which also contains the machine coding for the control computer.

Data on the magnetic field was taken at Kitt Peak during the first and second manned Skylab missions. Due to construction of a new solar magnetic field measuring facility at Kitt Peak maintenance of the main Kitt Peak Solar telescope suffered. Unfortunately during the period of reduced maintenance the main heliostat drive developed severe shake problems in light to moderate winds. The amplitude of the oscillation of the image was often 30 arc seconds and could exceed an arc minute. Because the oscillations were an appreciable fraction of a sun spot diameter there was little point to observing during the third manned mission.

In addition to the data taken at Kitt Peak, Lockheed Observatory operated its multislit spectrograph during the Skylab mission. On 5 September 1973 at 18:00 UT there was a class 1B flare that was well covered by the Skylab instruments as well as the Lockheed multislit system. Because of the basic similarity of the multislit and the spectroheliograph data it was reasonably straightforward to produce densitometer tracings of the flare region. A description of the flare reduction procedure is contained in Part D of Section I.

The densitometer traces of the flare represent the first ground based record of the hydrogen alpha spectrum with such complete temporal and

spatial resolution. In order to demonstrate and properly illustrate the spatial and temperal development of the Hα flare a short movie has been produced. The movie includes the original multislit data and the tracings of the flare region. Part E of Section I is a description of the movie.

In addition to the solar useage of the densitometer we have actively encouraged use of the system by outside users and have made the operating system of the densitometer generally available. The manufacturer of the densitometer now distributes program TRACE as contained in Section III as the normal operating system for desk based PDP-11 systems. Two systems, one at JPL and the other at Nice Observatory in France, are in operation. The National Science Foundation has funded the University of California, Berkeley, to essentially duplicate the Lockheed system. The Naval Observatory Station at Flagstaff is also in the process of acquiring a duplicate of the Lockheed system.

Students and staff of the Universities of California and Southern California and the Center for Astrophysics have used the system. One of the users was able to trace an image tube echelle spectra. The automatic tracing of the echelle plate would have been impossible on any other densitometer. The special curve following routines that adjoin program TRACE 3 which make echelle tracing possible will be published shortly. When the routines are in final form they will be supplied to the TRACE user's group.

B. MEASUREMENT OF MAGNETIC FIELDS BY FOURIER TRANSFORM TECHNIQUES

1. INTRODUCTION

Although there are currently a number of instruments that measure the longitudinal component of the solar magnetic field, there are very few systems that attempt to measure the vector field. The measurement of the vector field can be especially difficult in and around sunspots. We shall present in this paper a method for the measurement of the vector field in high field regions. The method is based on the fourier transform properties of circularly and linearly polarized spectra arising from simple Zeeman triplets.

Beckers[1] has briefly noted that Fourier spectroscopy and the resulting fourier transformed profiles are useful for directly determining field properites. In the discussions below we will amplify on the advantages and some of the shortcomings of the analysis of the transformed profiles. It will be demonstrated that when Zeeman splitting is on the order of half of the full width at half maximum (FWHM) of the basic line profile, then the magnitude of the field, the inclination of the field, the azimuthal angle of the field, and the velocity can be determined independent of the shape of the line profile, if the line profile obeys certain reasonable assumptions. In the sections on analysis of the errors in the fourier transform method, what constitutes a reasonable line profile will be discussed.

The methodology presented here has been successfully implemented. The basic data are pairs of spectra in right and left circular polarized light and three pairs of orthogonal linear polarizations. The data acquisition system is called a spectra-spectroheliograph and has been discussed in some detail by Title and Andelin[2]. Data are microdensitometered and digitized using a filter densitometering system described by Schoolman[3]. The digitized data are organized, reduced to absolute intensities, and analyzed with a set of programs described by November[4]. In this paper we shall not present actual magnetograms. The magnetograms will be discussed in a series of papers on the vector field in sunspots.

2. FOURIER TRANSFORM PROPERTIES

Circular Polarizations

For a normal absorption Zeeman triple in unpolarized light, the profile has the form:

$$p(\lambda-\lambda_o) = M(\lambda) - A'[f(\lambda-\lambda_o+\Delta) + h(\lambda-\lambda_o-\Delta)] - B\, g(\lambda-\lambda_o), \qquad (1)$$

where λ_o is the central wavelength of the line in the absence of a field; $M(\lambda)$ is the continuum intensity; f,h and g are the individual profiles of the displaced and undisplaced components; Δ is the Zeeman splitting; and A' and B are parameters that depend on the angle of the field and the properties of the atmosphere.

In the region of a line, we shall assume a constant continuum intensity. Then, for convenience, we drop the constant and treat the profile as an emission profile. Further, we shall assume:

$$f(\lambda-\lambda_o) = g(\lambda-\lambda_o) = h(\lambda-\lambda_o), \qquad (2)$$

and that the profiles are symmetric:

$$f(\lambda-\lambda_o) = f(\lambda_o-\lambda). \qquad (3)$$

Using assumptions (2) and (3) and dropping the continuum intensity, the Zeeman profile observed in unpolarized and right and left circularly polarized light can be written:

$$p(\lambda-\lambda_o) = A'[f(\lambda-\lambda_o+\Delta) + f(\lambda-\lambda_o-\Delta)] + B\, f(\lambda-\lambda_o) \qquad (4)$$

$$p\begin{pmatrix}RCP\\LCP\end{pmatrix} = \begin{pmatrix}A\\C\end{pmatrix} f(\lambda-\lambda_o+\Delta) + \begin{pmatrix}C\\A\end{pmatrix} f(\lambda-\lambda_o-\Delta) + B\, f(\lambda-\lambda_o) \qquad (5)$$

where

$$A' = A + C.$$

The fourier transforms of equations (4) and (5) are:

$$p(t) = [2(A+C)\cos\Delta t + B]\,\tilde{f}\,(t) \tag{6}$$

$$p_{\binom{RCP}{LCP}}(t) = [(A+C)\cos\Delta t + B]\,\tilde{f}\,(t) \pm i(A-C)\sin\Delta + \tilde{f}\,(t), \tag{7}$$

where:

$$\tilde{f}\,(t) = \int_{-\infty}^{\infty} f(u)\, e^{iut}\, du. \tag{8}$$

The tilde indicates a fourier transformed function. A catalog of circularly polarized profiles and the real and imaginary parts of their fourier transform is contained in Appendix I.

If the fourier transform of the basic profile (equation 8) does not have any zero crossings, and the field is not purely transverse (i.e., $A \neq C$), then the first zero of the imaginary part of the fourier transform of either circularly polarized profile yields the separation of the Zeeman components. That is, at:

$$\Delta t_1 = \pi,$$

$$\sin \Delta t_1 = 0$$

and

$$\Delta = \pi/t_1. \tag{9}$$

Since delta is directly proportional to the magnitude of the field strength, the zero crossing of the imaginary part directly determines the field strength. The fourier transforms of common profile functions, Lorentzian, Gaussian and Voight profiles, have no zero crossings.

If (A+C) is greater in magnitude than B, then the real part of equation (7) or equation (6) can be used to obtain the field strength. Since (A+C) is greater than B, the first zero occurs when:

$$\Delta t_2 = \pi/2 + \epsilon, \tag{10}$$

and the second zero when:

$$\Delta t_3 = \frac{3}{2}\pi - \epsilon, \tag{11}$$

where ϵ is smaller than $\pi/2$.

Hence,

$$\Delta = \frac{2\pi}{(t_2 + t_3)} \cdot \tag{12}$$

In addition, the fourier transform of the circular polarized profiles readily yields the inclination of the field. The slope at the origin of the imaginary part of either circular polarization transform (equation 7) is:

$$C_1 = (A-C)\ \Delta\ \tilde{f}\ (o), \tag{13}$$

while the value of the real part of the transform at the origin is:

$$C_o = (A+B+C)\ \tilde{f}\ (o). \tag{14}$$

The ratio of C_1 to C_o is then independent of the profile shape:

$$C_1/C_o = \frac{(A-C)}{(A+B+C)}\ \Delta. \tag{15}$$

Since delta is known from the value of the zero crossing, a quanity SS may be defined such that

$$SS = C_1/C_o\ \Delta$$

$$SS = \frac{(A-C)}{(A+B+C)} \cdot \tag{16}$$

The value of $\Delta t_1/2$ is $\pi/2$, hence the cosine at $\Delta t_1/2$ is zero while the sine is unity. Therefore, the ratio of the real and imaginary parts of equation (7) yields:

$$C_2 = \pm\left(\frac{B}{A-C}\right) \cdot \tag{17}$$

Again, using the assumption that (A+C) is greater than B, the first zero of the real part of the transform occurs when:

$$\cos(\Delta t_2) = \left(\frac{-B}{A+C}\right). \tag{18}$$

Combining (17) and (18), we obtain:

$$C_3 = (\mp) \left(\frac{A-C}{A+C}\right). \tag{19}$$

For most models of line formation, the quantity C_3 is directly related to the cosine of the angle of inclination. C_3 has the additional advantage that it is independent of the central component.

When the Seares' relations are valid,

$$A = 1/4\ (1 \pm \cos\gamma)^2 \tag{20}$$

$$B = 1/2\ \sin^2\gamma \tag{21}$$

$$C = 1/4\ (1 \pm \cos\gamma)^2, \tag{22}$$

where γ is the inclination of the field to the line of sight.

Using Seares' relation, result (16) is just:

$$SS = \cos\gamma. \tag{23}$$

Besides yielding the magnitude and inclination of the field, the sum of the right and left circular polarizations determine the Doppler shift. The fourier transform of the sum (the unpolarized Zeeman profile), is a symmetric function about the central wavelength of the profile. Hence its transform is real. Therefore, the fourier transform with respect to any other wavelength λ_s must be of the form:

$$\tilde{p}_s(t) = e^{ist}\,\tilde{p}(t), \tag{24}$$

where

$$s = \lambda_s - \lambda_o. \tag{25}$$

Since p(t) is real, the inverse tangent of the ratio of the imaginary and real parts of $p_s(t)$ yields the offset, s:

$$s = \tan^{-1} [\text{Imag } (\tilde{p}_s[t]) \; / \; \text{Real}(p_s[t]) \;]. \tag{26}$$

The velocity shift with respect to the undisplaced wavelength λ_o is:

$$v = sc/\lambda_o, \tag{27}$$

where c is the velocity of light.

Linear Polarizations

Using the same assumptions as used in equation (4) for circularly polarized light, Zeeman profiles observed through a linear polarizer at angle phi with the projection of B in the azimuthal plane has the form

$$p_\varphi(\lambda) = E_\varphi [f(\lambda-\lambda_o+\Delta) + f(\lambda-\lambda_o-\Delta)] + F_\varphi \; f(\lambda-\lambda_o), \tag{28}$$

where E_φ and F_φ are functions of gamma and phi. The fourier transform of equation (28) is:

$$\tilde{p}_\varphi(t) = [2E_\varphi \cos \Delta t + F_\varphi \;] \; \tilde{f}(t). \tag{29}$$

In the case that Unno's relations[6] hold:

$$E_\varphi = \alpha/4(1 + \cos^2 \gamma - \sin^2 \gamma \sin 2\varphi) \tag{30}$$

$$F_\varphi = \beta/2(1 + \sin 2\varphi) \sin^2 \gamma \; , \tag{31}$$

where α and β are functions of the absorption parameters that describe the line and of the angle γ. For weak lines, α and β are unity.

It is useful to analyze the sum and difference of orthogonal pairs of linearly polarized profiles. Using relations (30) and (31), the sum and difference transforms are:

$$\tilde{p}_{S\,\varphi}(t) = [\alpha(1 + \cos^2\gamma)\cos\Delta t + \beta\sin^2\gamma]\,\tilde{f}(t), \tag{32}$$

$$\tilde{p}_{D\,\varphi}(t) = [-\alpha(\sin^2\gamma\sin 2\varphi)\cos\Delta t + \beta\sin^2\gamma\sin 2\varphi]\,\tilde{f}(\epsilon). \tag{33}$$

A catalog of linear polarization profiles and their sum and difference fourier transforms is contained in Appendix II.

If β is less than or equal to α, the sum transform will be zero for the values of t symmetric about $\Delta t = \pi$. That is, at:

$$\Delta t_3 = \pi - \epsilon\ ,$$

and $$\Delta t_4 = \pi + \epsilon,$$

the sum transform is zero. Hence:

$$\Delta = \pi/(t_3 + t_4). \tag{34}$$

Then, given the value of Δ, the sum and difference transforms can be compared at t_2 such that Δt_2 is $\pi/2$. Then:

$$\left.\frac{p_{S\,\varphi}}{p_{D\,\varphi}}\right|_{\Delta t_2=\pi/2} = \sin 2\varphi\ . \tag{35}$$

Hence, a pair of linear polarizations can yield the azimuthal angle of the field. Because of the possibility that the field is 0 or 90° (parallel or perpendicular) to the analyzer, it is useful to analyze several orthogonal pairs. Also, since the sum profile is a symmetric function, the velocity shift can also be obtained with a pair of linear polarizations.

3. ACCURACY AND LIMITATIONS OF THE FOURIER TRANSFORM METHOD

Total Field Strength

From the discussion above, the magnitude of the magnetic field, the angle to the line of sight, the azimuthal projection, and the line of sight velocity are readily available from the fourier transforms of the line profiles. However, as with any measurement method, there are problems that occur because of both random and systematic errors. The fourier transform method is remarkably insensitive to some classes of error or noise and sensitive to others.

The measurement of Δ, and hence the total field strength, $|B|$, is straightforeward. It depends only on the zero crossing of the imaginary part of the circular polarization transform. The accuracy of the zero crossing technique increases as the magnetic splitting increases with respect to the width of the basic profile. The fundamental reason for the improvement in accuracy with large splitting to width ratio is that the larger the splitting, the lower the spatial frequency at which the zero crossing occurs, while the narrower the profile, the higher in spatial frequency its transform has significant amplitude. Because of its fundamental importance, the ratio of splitting to full width at half maximum (FWHM) shall be defined as:

$$Q = \Delta/\mathrm{FWHM}. \tag{36}$$

The amplitude of the imaginary part of a circular polarization transform is proportional to cosine gamma. Thus, the zero crossing determination will also depend on cosine gamma.

In order to get some measure of the effectiveness of the transform technique, a program was written to create artificial profiles that could then be subjected to various sytematic and random effects that

simulate some solar and measurement problems. To check the validity of the zero crossing procedure, Zeeman profiles were constructed using the Sears relations and Gaussian and Lorenzian profiles. The profiles so constructed were subjected to random noise proportional to the maximum signal value of the undisturbed profile. These synthetic profiles were then transformed and analyzed for the first zero crossing. By repeated evaluation of the same profile subjected to random noise, it was possible to calculate the standard deviation of the zero crossing versus percentage noise in the profile. The procedure was carried out for a variety of gammas and splitting-to-width ratios for both Gaussian and Lorentzian line shapes.

Upon completion of the analysis, it was found that, if the error in the zero crossing was normalized by cosine gamma, the percent error of the zero crossing was a function only of the ratio of the splitting to the width of the line profile, so that for a noise $n(P_{max})$ in the profile:

$$N_B \frac{n(B)}{B} = \frac{n(P_{max})}{P_{max}} N \cos \gamma, \qquad (37)$$

where N_B is the noise reduction and $n(B)$ is the standard deviation in the measurement of B. Shown in Figure 1 is the noise reduction factor, the ratio of the noise in the profile to the noise in the zero crossing, versus Q, the ratio of the splitting to the full width at half maximum (FWHM) for Gaussian and Lorentzian profiles. From the figure it is seen that when the field is vertical at a magnetic splitting equal to FWHM, the noise in the measured field is reduced by a factor of 12 (Gaussian) from the noise in the profile. For a 60° inclination of the field, the reduction factor is 6 and for 75°, it is 3.

In order to measure $|B|$, the position of the unpolarized line center must be known accurately because an error in the center position will be reflected as an error measured in the splitting. For a pure longitudinal field, an error in the line center position will cause an

error of equal magnitude in the splitting for a single circular polarization. However, the centering error will cause an equal but opposite error in the splitting inferred from the opposite circular polarization. Thus, at least for longitudinal field, the mean splitting obtained from the sum of the right and left circular profiles will have the correct value.

For other than pure longitudinal fields, the centering error is somewhat more complex. From equation (24) in the presence of a centering error, s, and a splitting, Δ, the condition for the zero of the imaginary parts of the transform is:

$$A\ \mathrm{sint}(s + \Delta) + C\ \mathrm{cint}(s - \Delta) + B\ \mathrm{sints} = 0. \tag{38}$$

Since, in the absence of a centering error, the zero of the imaginary part occurs when:

$$\Delta t_1 = \pi,$$

in the presence of a small error condition (38) occurs when

$$\Delta t_s = \pi + \zeta t, \tag{39}$$

where ζ is just the splitting error.

Substituting (39) into (38) yields the relation between the centering and splitting error:

$$\Delta\ \mathrm{sint}(s + \zeta) + C\ \mathrm{sint}(s - \zeta) - B\ \mathrm{sints} = 0. \tag{40}$$

If the errors are small, then:

$$\zeta = \frac{(A + C - B)}{(A - C)}\ s. \tag{41}$$

Using the Seares relations, equation (40) becomes:

$$\zeta = \pm(\cos \gamma)s. \tag{42}$$

From results(41) and (42), the splitting error averages to zero when the splittings obtained from the right and left circular polarizations are averaged. Further when Seares relations hold, the error in $|B|$ caused by a centering error is diminished by the cosine of the inclination.

One of the assumptions of the fourier transform technique is that all three of the Zeeman components have the same profile shape. However, if the undisplaced profile is symmetric it may differ from the shape of the displaced components without affecting the value of the zero crossing because the imaginary part of the circular transform is free of all profile components that are symmetric about the profile center. The lack of dependence on the central component is very useful because it means scattered photospheric light or the existence of molecular lines centered on the profile do not affect the value of $|B|$.

Another transform assumption is that the profile shape is symmetric about the undisplaced center. There are at least two physical conditions which can cause line profile asymmetry - magnetic field gradients and velocity field gradients. Magnetic field gradients cause mirror asymmetry in the displaced profiles. That is, the profile displaced to high wavelengths is the mirror image of the component shifted to shorter wavelengths. In the case of the mirror asymmetry, the profile can be considered to be made of a sum of profiles that are shifted by differing amounts. Since the fourier transform procedure is a linear process, the zero crossing will reflect a weighted average magnetic splitting. In the case of a velocity gradient asymmetry, all three profiles are asymmetric in the same direction. The first effect of a velocity gradient will be an error in the center wavelength of the sum line profile. As discussed above, if

simultaneous profiles are obtained in right and left circular polarizations, the velocity error will increase the field estimated from one profile and decrease the field from the other. The order of the error will be the same, so that the average of the right and left circular polarization fields will be a good estimate of $|B|$ and the difference will be a measure of the velocity gradient error.

Even if the line profiles are symmetric and well centered, the fourier transform can still yield erroneous results for $|B|$ if there exist photometry errors. To get an idea of the magnitude of this error, profiles of the form:

$$p_\delta(\lambda) = p(\lambda)^{1+\delta} \tag{43}$$

were analyzed. It is clear that for pure longitudinal fields that the value of the zero crossing is unaffected by δ. However, as the field inclination increases, the effect of non-zero δ on the zero crossing increases. On the other hand, as Q increases, the effect of non zero δ should decrease, since the profile components overlap region decreases. Shown in Figure 2 are plots of percent error in the zero crossing versus inclination of field for $\delta = -.05$ and $-.1$ for $Q = .5$. Shown in Figure 3 are plots of percent error in the zero crossing verus Q for the same values of δ for a field inclination of 82°. Negative values of δ cause an increase in the splitting values while positive values cause a decrease of splitting. For values of $\delta < |.08|$ the magnitude of the crossing error is nearly independent of sign of δ. Note that the values of Q and γ used in Figures 2 and 3 respectively were chosen to illustrate maximal error sensitivity.

In practice, it should be possible to correct the photometry so that the error in δ is less than $|.05|$.

4. THE INCLINATION OF THE FIELD

Once the value of $|B|$ is known, the inclination can be determined as indicated by the series of results (17), (18) and (19). Result (19) yields cosine γ independent of the value of the central component and

only requires Unno's relations to hold. However, since result (19) is independent of the central component, it cannot be expected to be of much value for small values of the ratio A/C. For inclinations of less than 45°, $A/C < .03$. But by 60°, $A/C = .11$. Thus, it should not be surprising if the accuracy of cosine γ markedly deteriorates at inclinations of less than 45°.

For angles of inclination less than 45°, the slope at the origin of the imaginary part of the transform can be utilized. However, not only does this method require that Seares relation hold, but perhaps more importantly, introduces dependence on the strength of the possibly contaminated central component. Another method of obtaining cosine γ is to take advantage of the properties of linear polarization transforms, since these depend on sine gamma.

The method used to obtain result (19) can be improved upon. Since the value of Δ is known, the ratio of the real to the imaginary part of the transform can be multiplied by sin Δ t to create a function:

$$RS(t) = \frac{(A+C)\ \cos t\Delta + B}{(A-C)} \ . \qquad (44)$$

The integral of the product of $RS(\Delta t)$ and the first two Legendre polynomials properly normalized over the range in Δt for 0 to π yield

$$\int RS(\Delta t)\ d(\cos\Delta t)\ P_o = \left(\frac{B}{A+C}\right) \qquad (45)$$

$$\int RS(t)\ d(\cos\Delta t)\ P_1 = \left(\frac{A+C}{A-C}\right) \ . \qquad (46)$$

Since the Lengendre polynomials are orthogonal functions, the integrals of $RS(\Delta t)$ times higher order polynomials yield information on the degree of asymmetry and or differences between the central and displaced components in the line profiles.

The value of the integral approach of equation (46) is that a significant portion of the transformed function is used rather than the single point which is used for result (19). However, the formation of

$RS(\Delta t)$ entails dividing out a denominator that can take on zero values. By use of Gaussian quadrature, the points at which $RS(\Delta t)$ can become large can be avoided without loss of numerical accuracy. When the correlation coefficient of the error in $|B|$ and the error in cosine γ are evaluated from profiles subjected to random noise, for inclination greater than 45° and $Q > .5$, the correlation coefficient is less than .01.

Using the random synthetic profile program, the noise in cosine gamma was evaluated. As with the error in $|B|$, the noise in cosine γ is reduced by a factor normalized by cosine gamma. Thus, for an amount of noise $n(P_{max})$:

$$N_\gamma \frac{n(\cos\gamma)}{\cos\gamma} = \frac{n(P_{max})}{P_{max}} \cos\gamma, \tag{47}$$

and

$$n(\cos\gamma) = \frac{n(P_{max})}{P_{max}\, N_\gamma} . \tag{48}$$

Thus, the error in cosine gamma is independent of gamma. Shown in Figure 4 is a plot of N_γ versus Q. Relations (47) and (48) hold for angles greater than 45°. For angles less than 45°, methods for determining cosine γ from result (46) fail.

Since it is not until slightly under 15° that the ratio:

$$A/B < .03,$$

it can be expected that result (23) is useful between 15° and 45° for determining cosine γ. Numerical experiment in fact shows that the slope of the imaginary part of the transform is useful for inclination less than 45°.

The polynomial measurement of cosine gamma is only weakly dependent on differences in shape between the central and displaced components, and errors introduced by such differences are manifested in the coefficients of the higher order Legendre polynomials in the expansion of $RS(\Delta t)$. Also, as with

$|B|$ errors in centering the line cause equal and opposite effects on the value of cosine gamma measured. As a consequence, the average value of cosine gamma will be a good estimate even in the presence of a centering error.

Photometry errors cause a somewhat different effect on cosine gamma than on the measurement of $|B|$. As shown in Figure 5, the percent error in cosine gamma versus inclination of field only slowly increases with angle, while as shown in Figure 6, the error in cosine gamma versus Q does not decrease with Q as does the error in $|B|$, but rather increases. Further, as seen from Figures 5 and 6, the size of the error in cosine Υ is only a slowly varying function of both gamma and Q. Shown in Figure 7 is a plot of the error in gamma versus gamma for a ten percent error in cosine Υ. Figure 7 deomonstrates that estimates of the inclination of larger angles are almost certainly correct while the accuracy of angles less than 40° is extremely sensitive to photometry.

5. DISCUSSION

From the arguments above there are two major advantages of the fourier transform method. The first is that the magnitude of the field can be measured independent of the shape of the profile. The second is that for large fields, the magnitude of the field can be measured with an accuracy which is a factor of 10 to 25 better than that of the basic line profile. Since measurement accuracy depends on the square of the number of photons counted, the factor of 10 to 25 increase in accuracy represents a factor 100 to 625 in observing time required.

The main disadvantage to the method is a possible systematic photometry error. At present, we can measure the field in sunspots relatively to an accuracy of about one percent, with a possible systematic error of 5 percent. Cosine γ can be measured relatively to 3 to 4 percent and absolutely to 8 to 10 percent.

The fourier transform method does not require a great deal of computer time. This is not because a fast fourier transform method is used, but rather because a relatively few fourier components need be evaluated to find the zero crossing. Usually less than ten fourier components must be evaluated. For just a few transforms it is sufficient to determine the sines and cosines recursively.

REFERENCES

1. Beckers, J.M., I.A.U. Symposium No. 43, Solar Magnetic Fields, R. Howard, ed., page I

2. Title, A.M., and J.P. Andelin, Jr., ibid, page 298

3. Schoolman, S., Program TRACE, Lockheed Report for NAS8-28018

4. November, L., Operator's Manual for Microdensitometer Program, Lockheed Final Report for NAS8-28018

5. Seares, F.H., "The Displacement-Curve of the Sun's General Magnetic Field," in Astrophys J. 30, 99

6. Unno, W., "Line Formation of a Normal Zeeman Triplet," Pub. Astron. Soc. Japan 8, 108, 1956

FIGURE CAPTIONS

Figure 1. Noise reduction in zero crossing from noise in profile data versus the ratio of splitting/FWHM. Curve (a) is for Gaussian profiles while (b) is for Lorenzian profiles.

Figure 2. Percent error in zero crossing versus inclination of the field for photometric errors of size δ, for $Q = .5$.

Figure 3. Percent error in zero crossing versus splitting FWHM for several photometric errors for a field inclination of 82.82° ($\cos \gamma = .125$).

Figure 4. Noise reduction in the measurement of cosine gamma versus splitting/FWHM.

Figure 5. Percent error in cosine gamma versus gamma for photometric errors of size δ for $Q = 1.5$.

Figure 6. Percent error in cosine gamma versus splitting/FWHM for photometric errors of size δ for a field inclination of 82.82°.

Figure 7. Percent error in angle versus angle for a 10 percent error in cosine gamma.

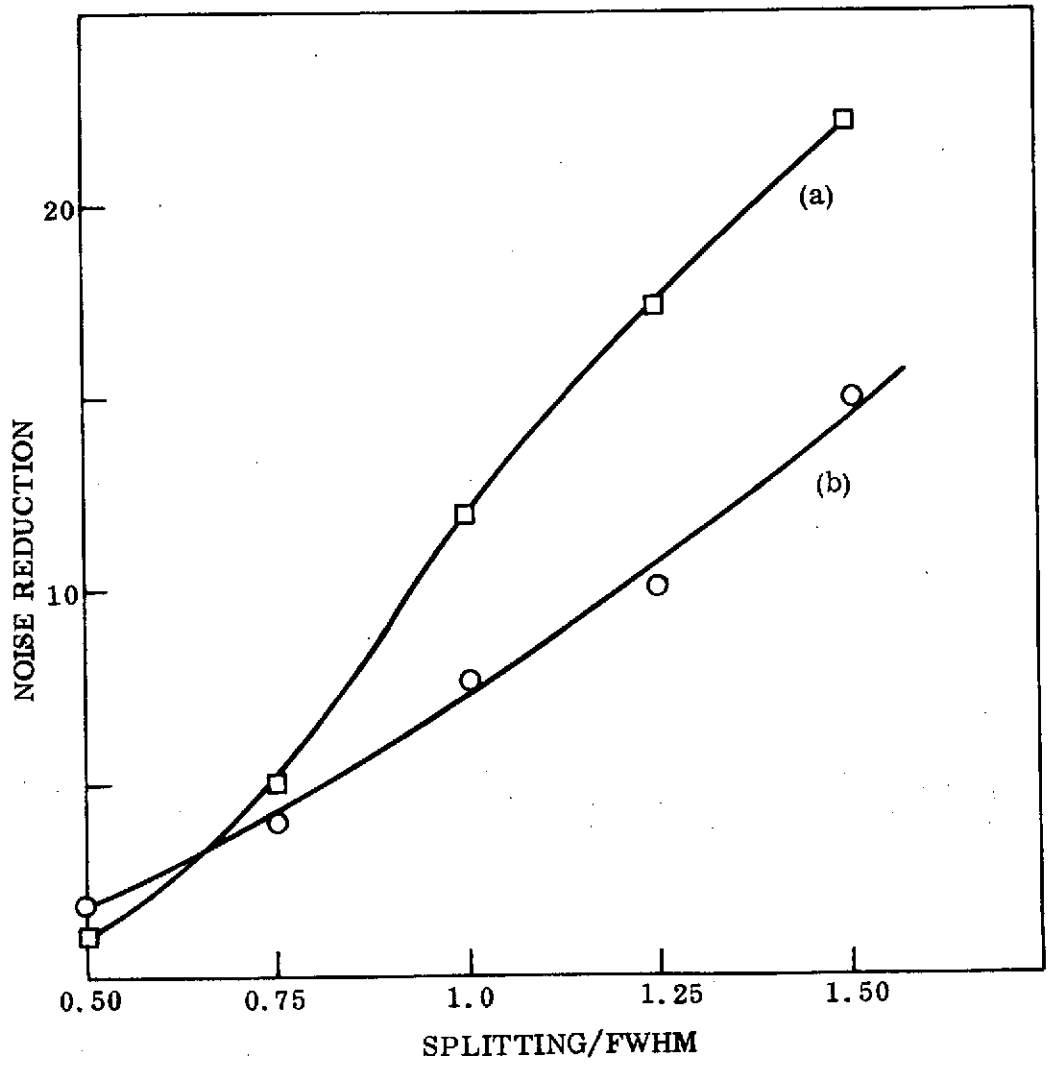

Figure 1

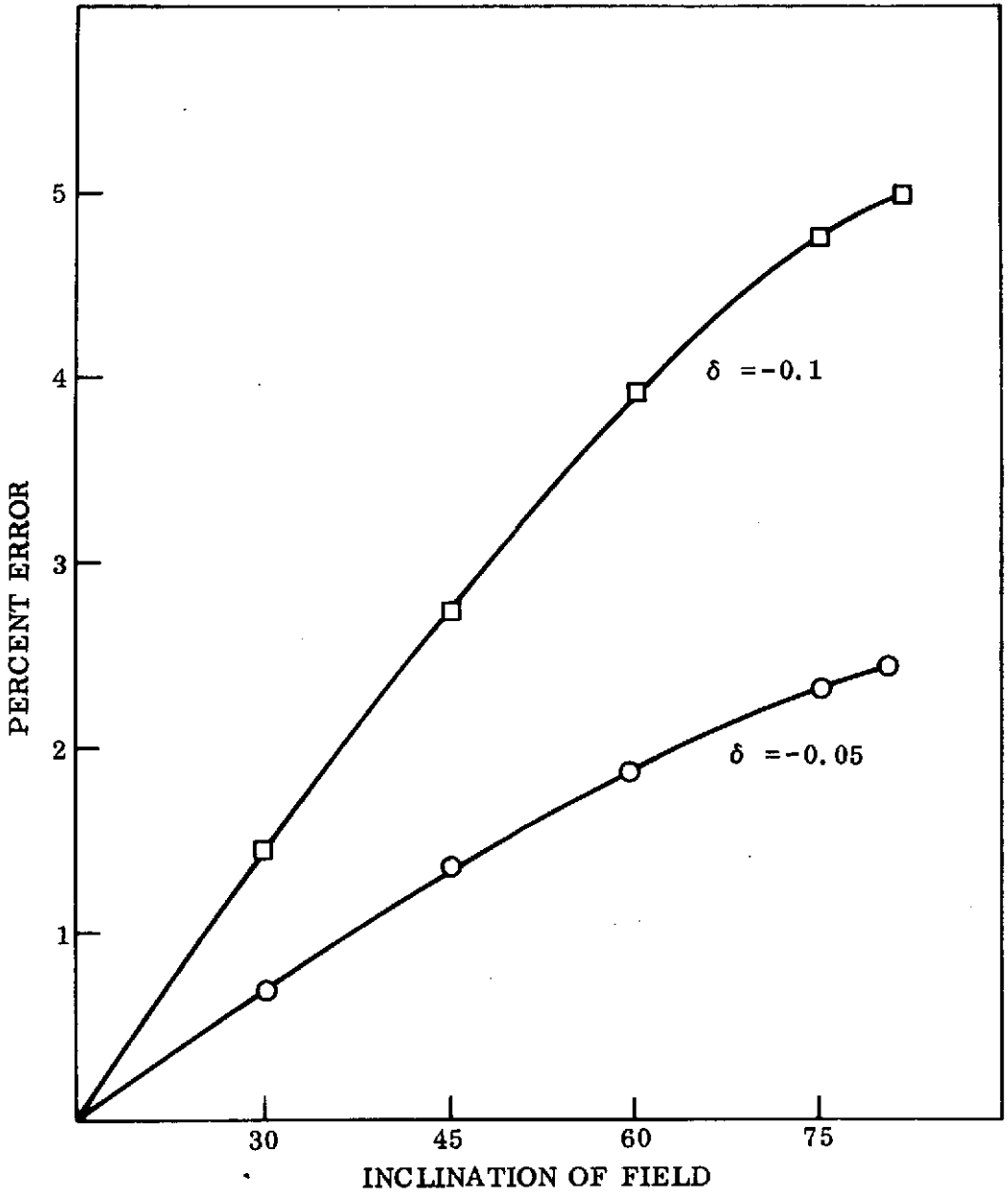
PERCENT ERROR
5
4
3
2
1
δ =-0.1
δ =-0.05
30
45
60
75
INCLINATION OF FIELD

Figure 2

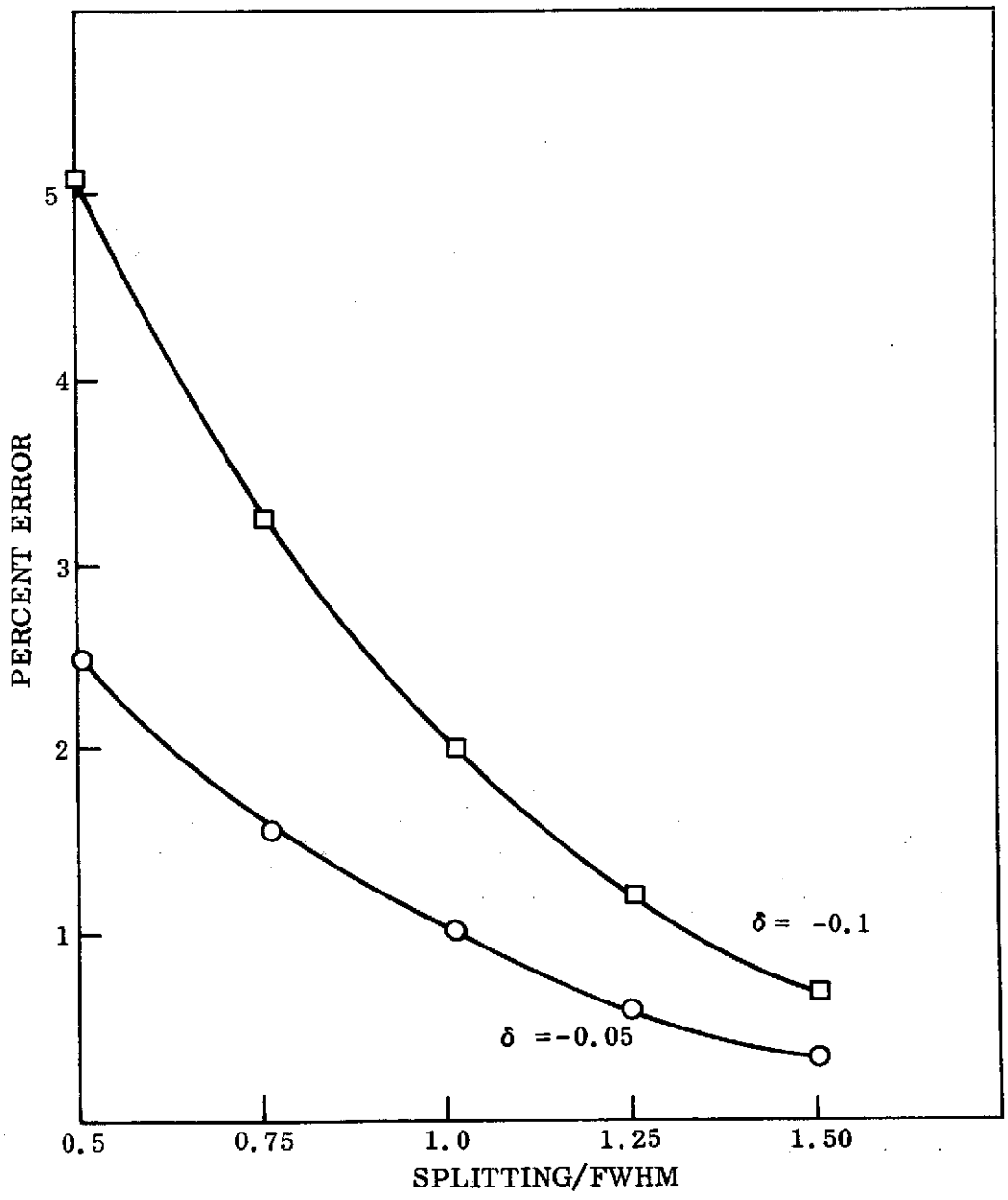
PERCENT ERROR
5
4
3
2
1
0.5
0.75
1.0
1.25
1.50
SPLITTING/FWHM
δ = -0.1
δ =-0.05

Figure 3

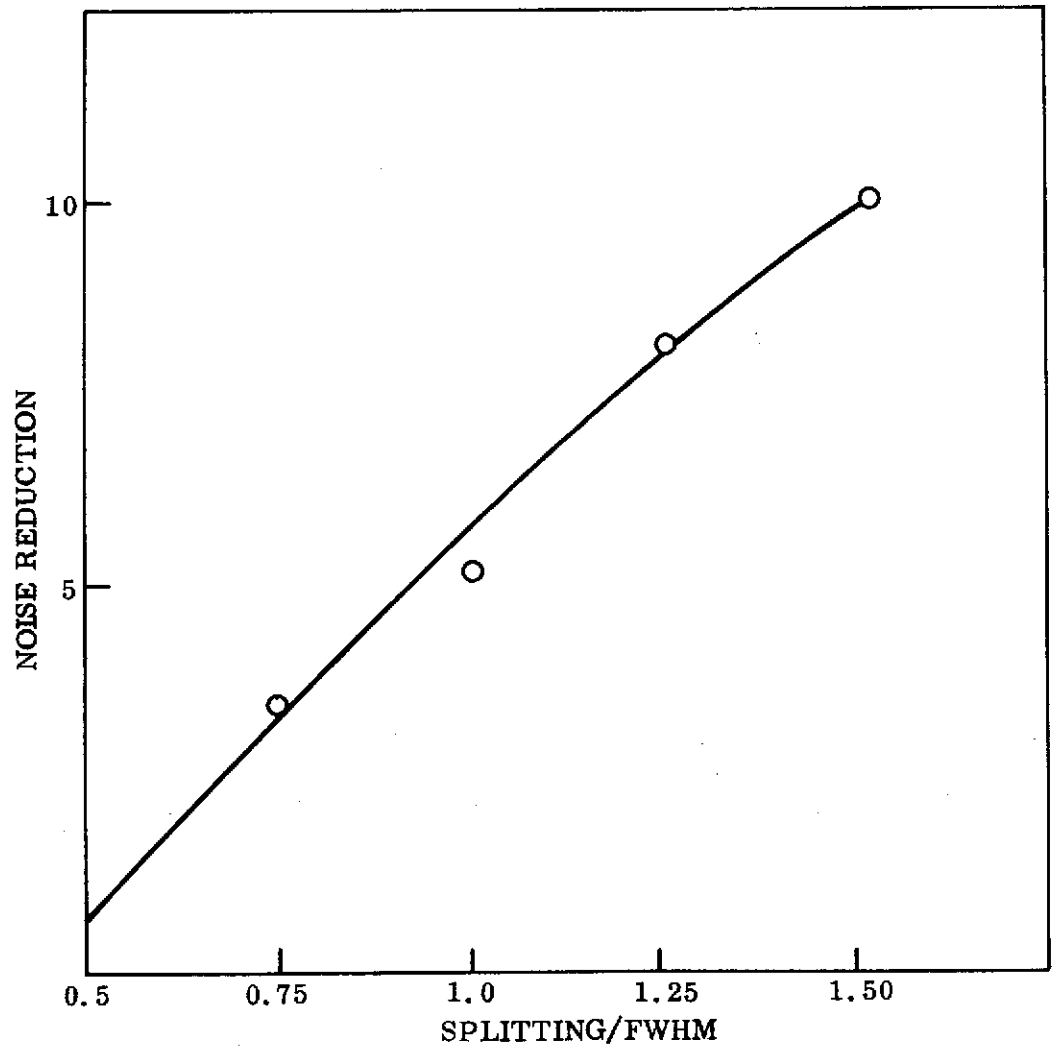

Figure 4

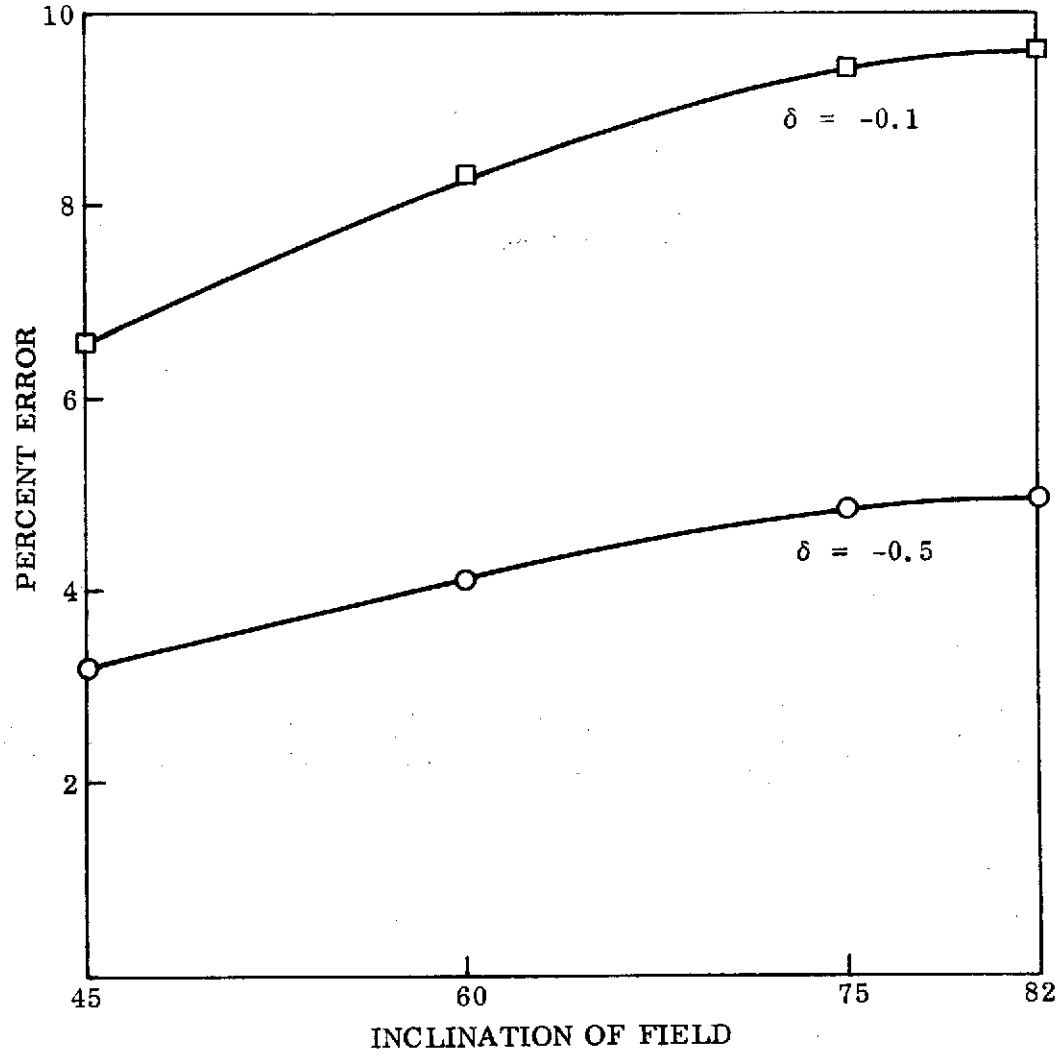
10
8
6
4
2
PERCENT ERROR
δ = -0.1
δ = -0.5
45
60
75
82
INCLINATION OF FIELD

Figure 5

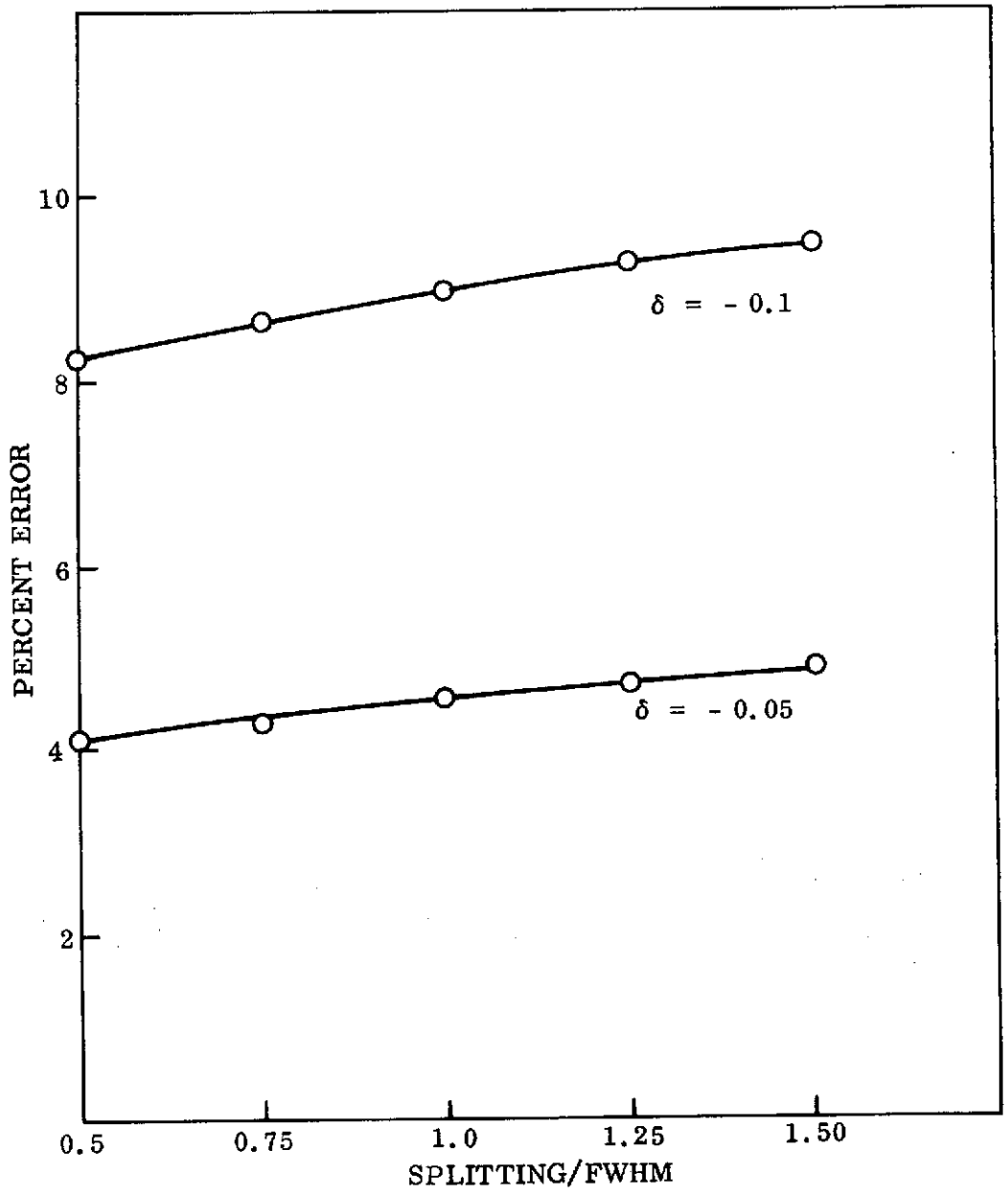
10
8
6
4
2
PERCENT ERROR
δ = - 0.1
δ = - 0.05
0.5
0.75
1.0
1.25
1.50
SPLITTING/FWHM

Figure 6

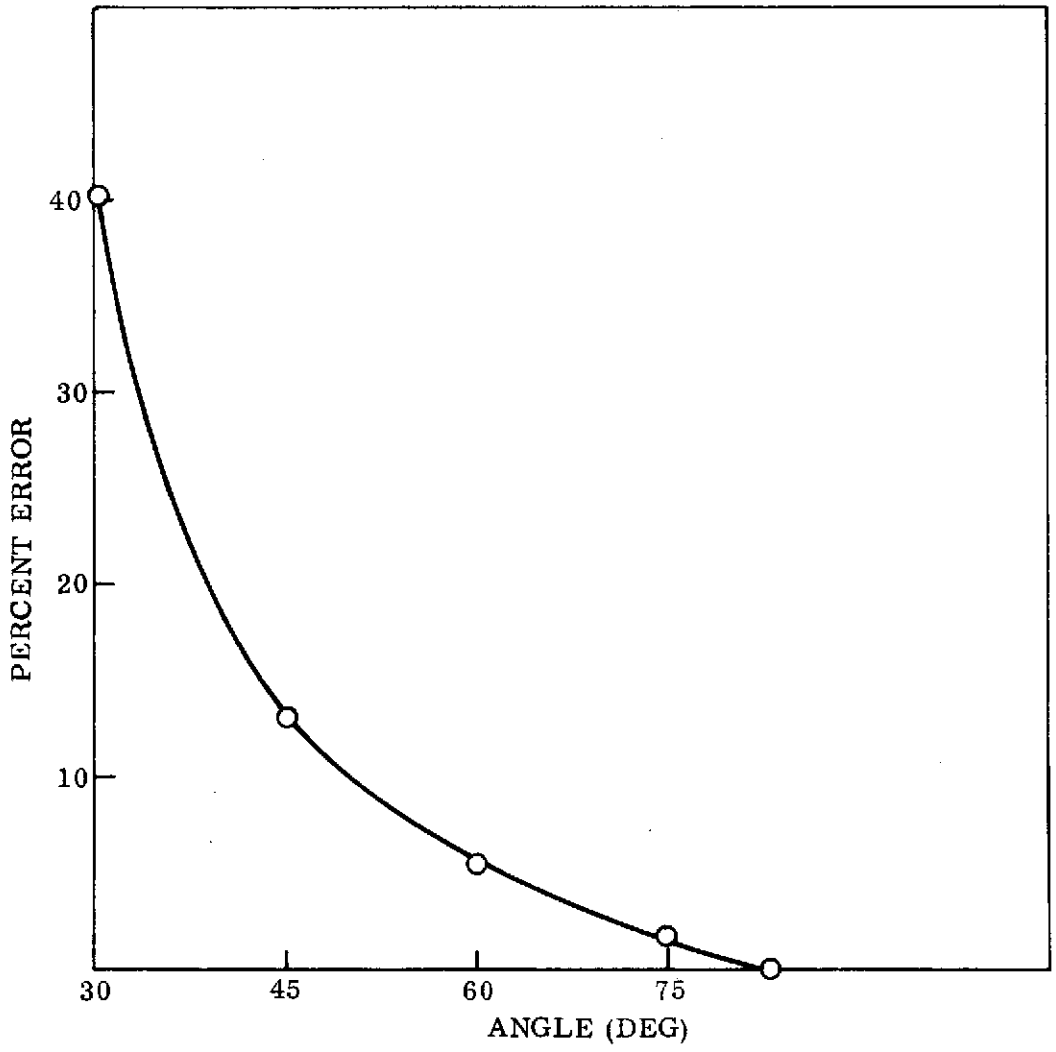

Figure 7

APPENDIX I

Shown in Figures A1 through A6 are plots of Gaussian based Zeeman profiles in a single circular polarization and the corresponding real and imaginary parts of the profiles' fourier transform. The set of figures include profiles with inclinations to the vertical from 0° to 75° in 15° steps of .25. Seares' relations were used for the relative amplitudes of the three Zeeman components. The profiles are normalized so that peak amplitude at zero inclination is unity. The transforms are normalized so that the amplitude of the real part of the transform is unity at zero spatial frequency. On an individual figure which covers a single field inclination each row contains a profile and the corresponding real and imaginary transforms. Successive rows on a given figure are for successively higher ratios of Q, the ratio of splitting to FWHM.

Figure A1

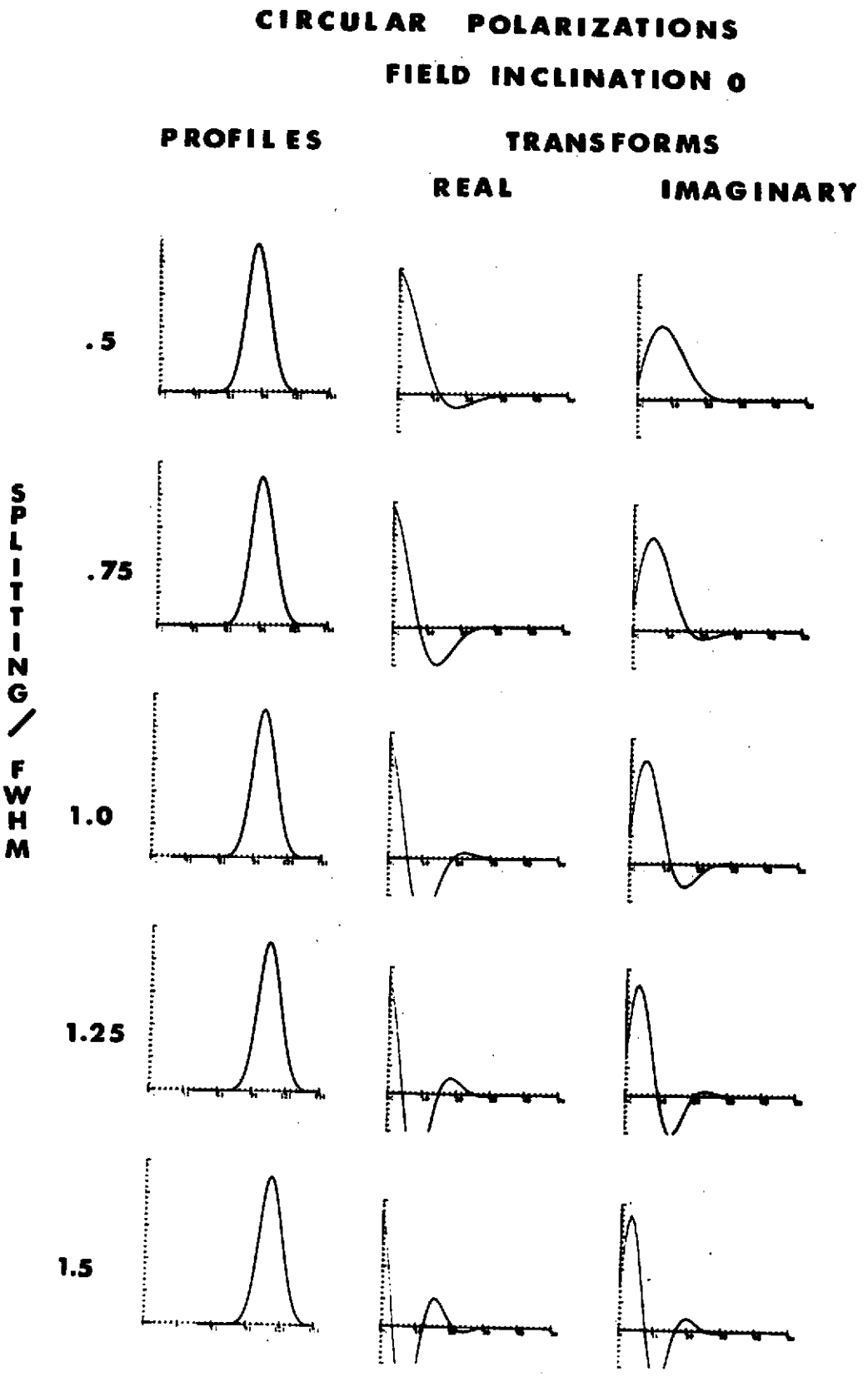
CIRCULAR POLARIZATIONS
FIELD INCLINATION 0
PROFILES
TRANSFORMS
REAL
IMAGINARY
SPLITTING / FWHM
.5
.75
1.0
1.25
1.5

Figure A2

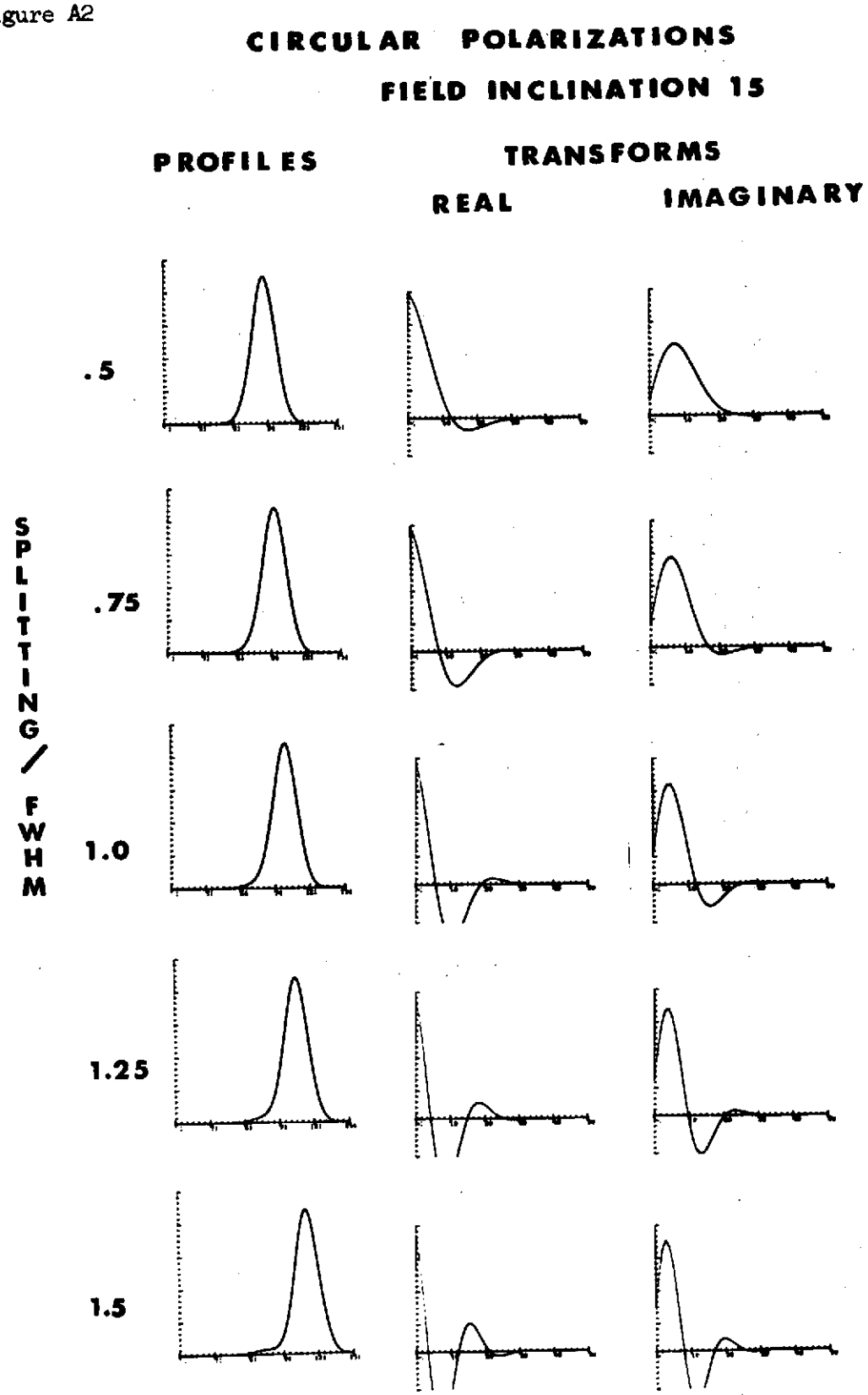
CIRCULAR POLARIZATIONS
FIELD INCLINATION 15
PROFILES
TRANSFORMS
REAL
IMAGINARY
SPLITTING / FWHM
.5
.75
1.0
1.25
1.5

Figure A3

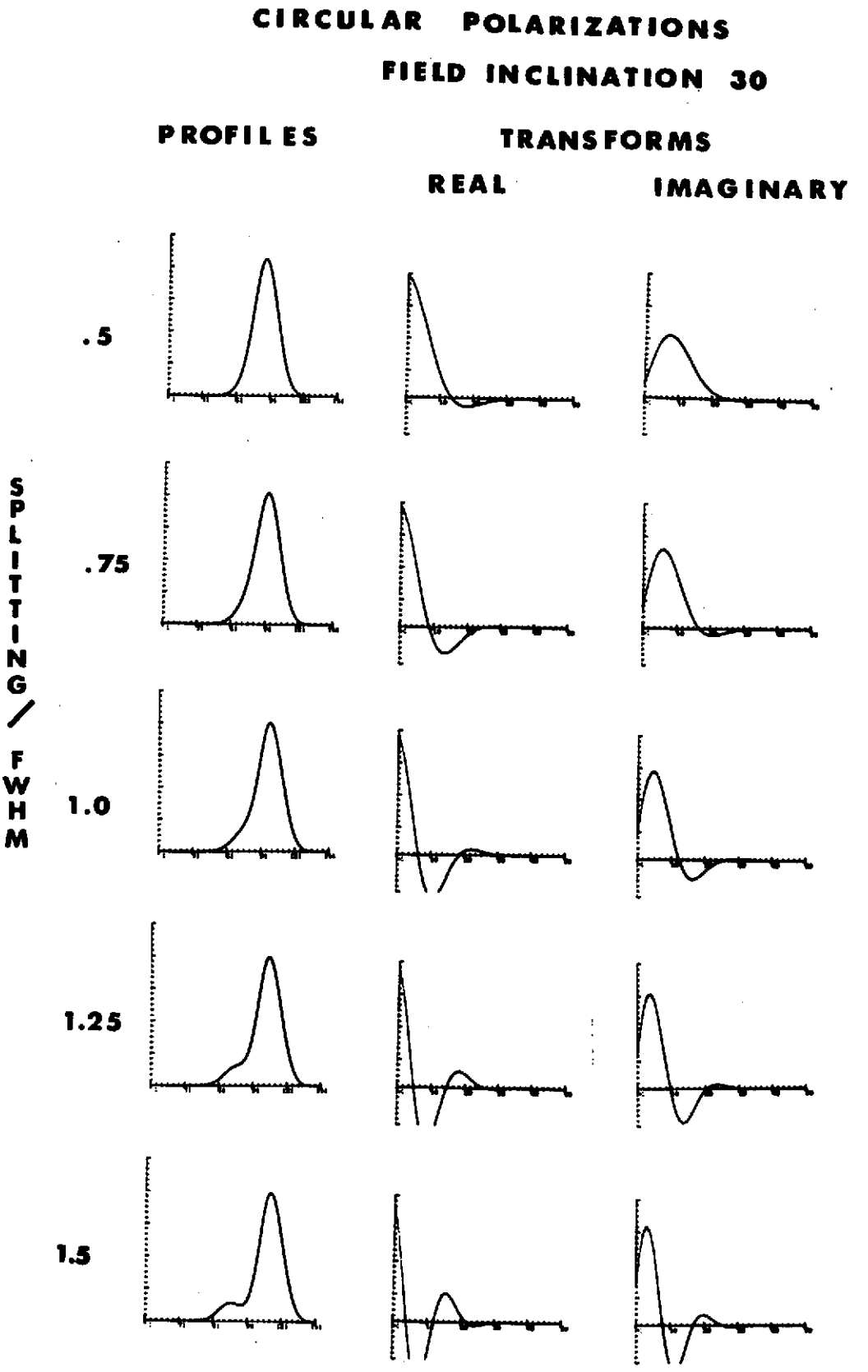
CIRCULAR POLARIZATIONS
FIELD INCLINATION 30
PROFILES
TRANSFORMS
REAL
IMAGINARY
SPLITTING / FWHM
.5
.75
1.0
1.25
1.5

Figure A4

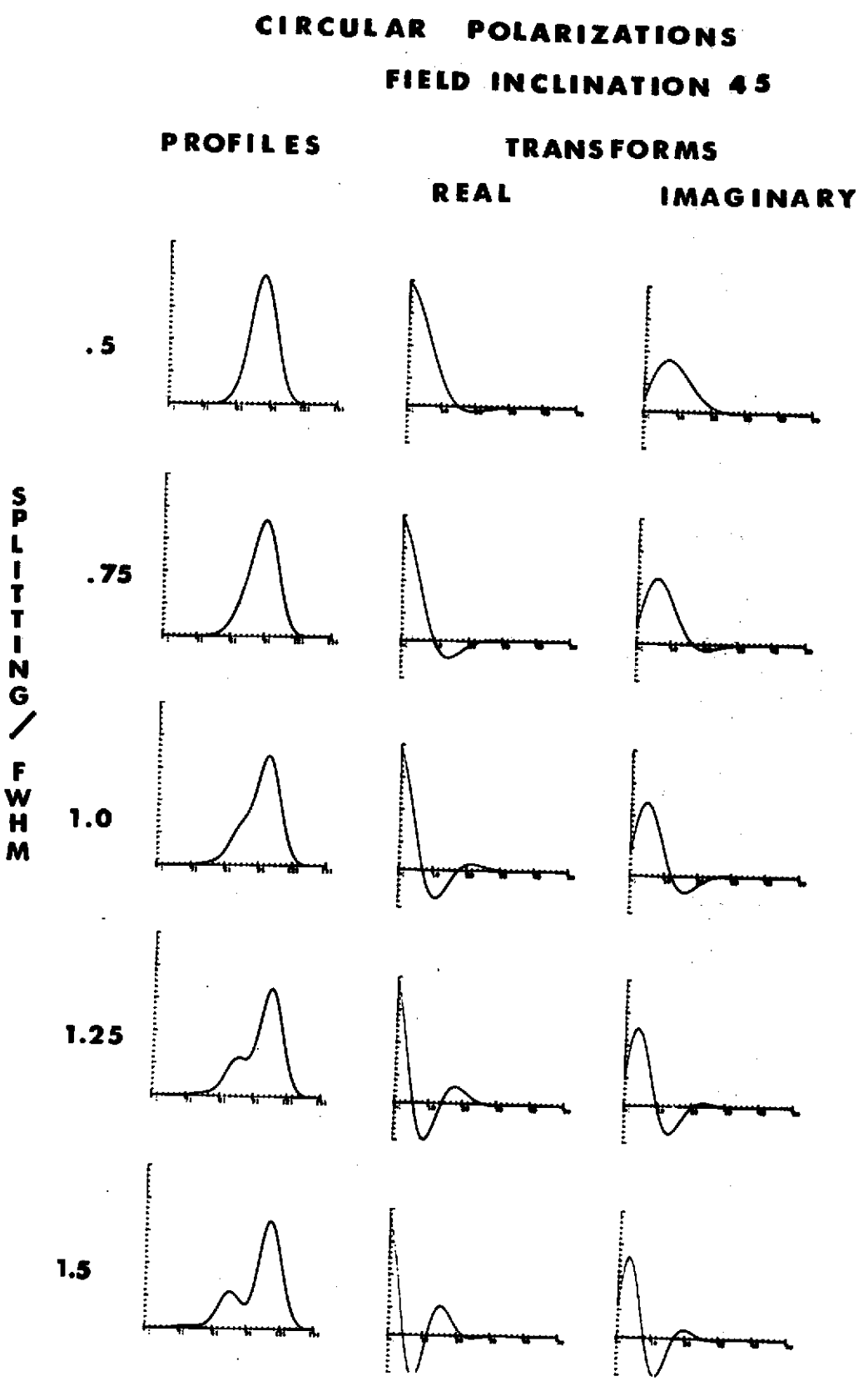
CIRCULAR POLARIZATIONS
FIELD INCLINATION 45
PROFILES
TRANSFORMS
REAL
IMAGINARY
SPLITTING / FWHM
.5
.75
1.0
1.25
1.5

Figure A5

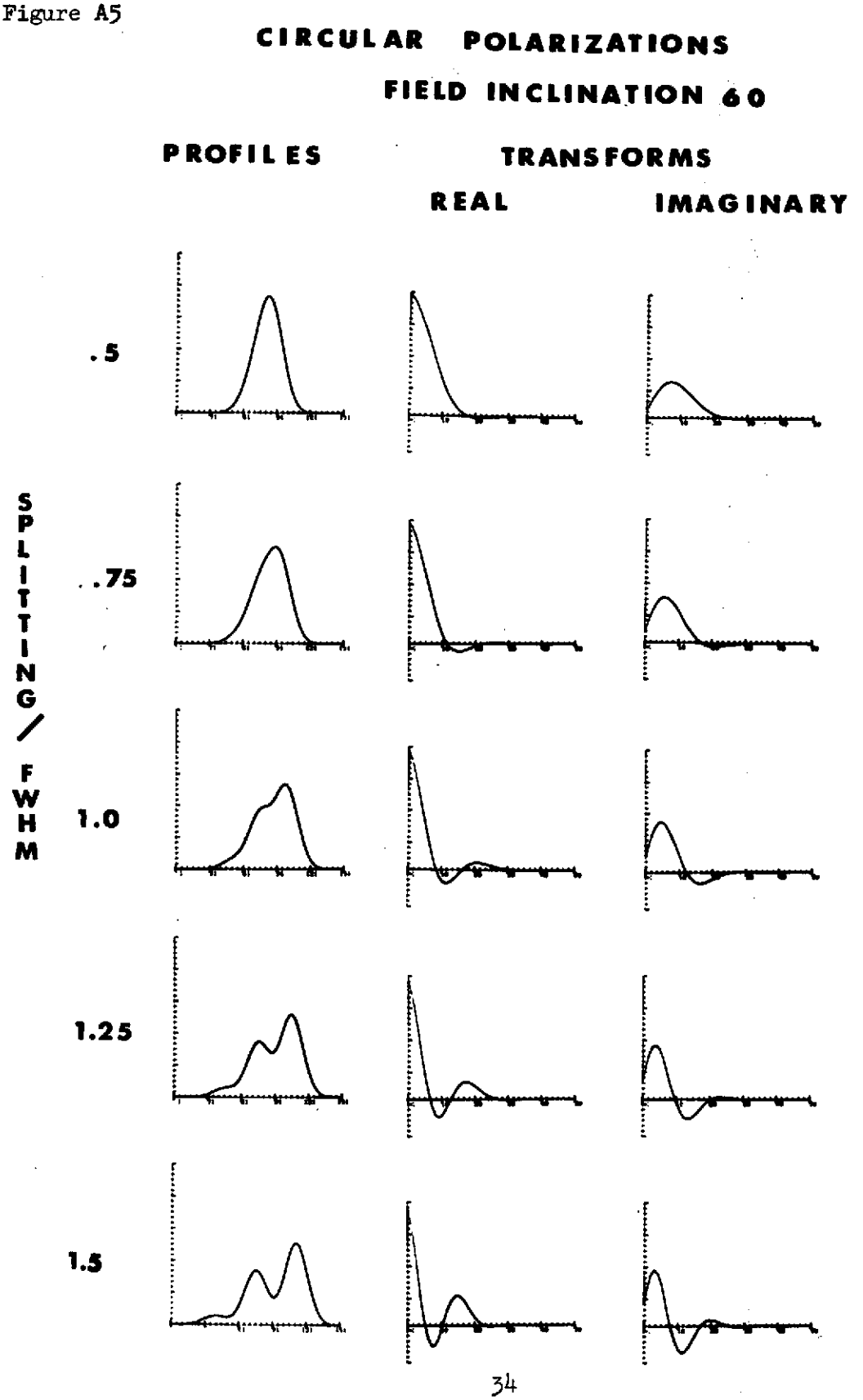
CIRCULAR POLARIZATIONS
FIELD INCLINATION 60
PROFILES
TRANSFORMS
REAL
IMAGINARY
SPLITTING / FWHM
.5
.75
1.0
1.25
1.5

Figure A6

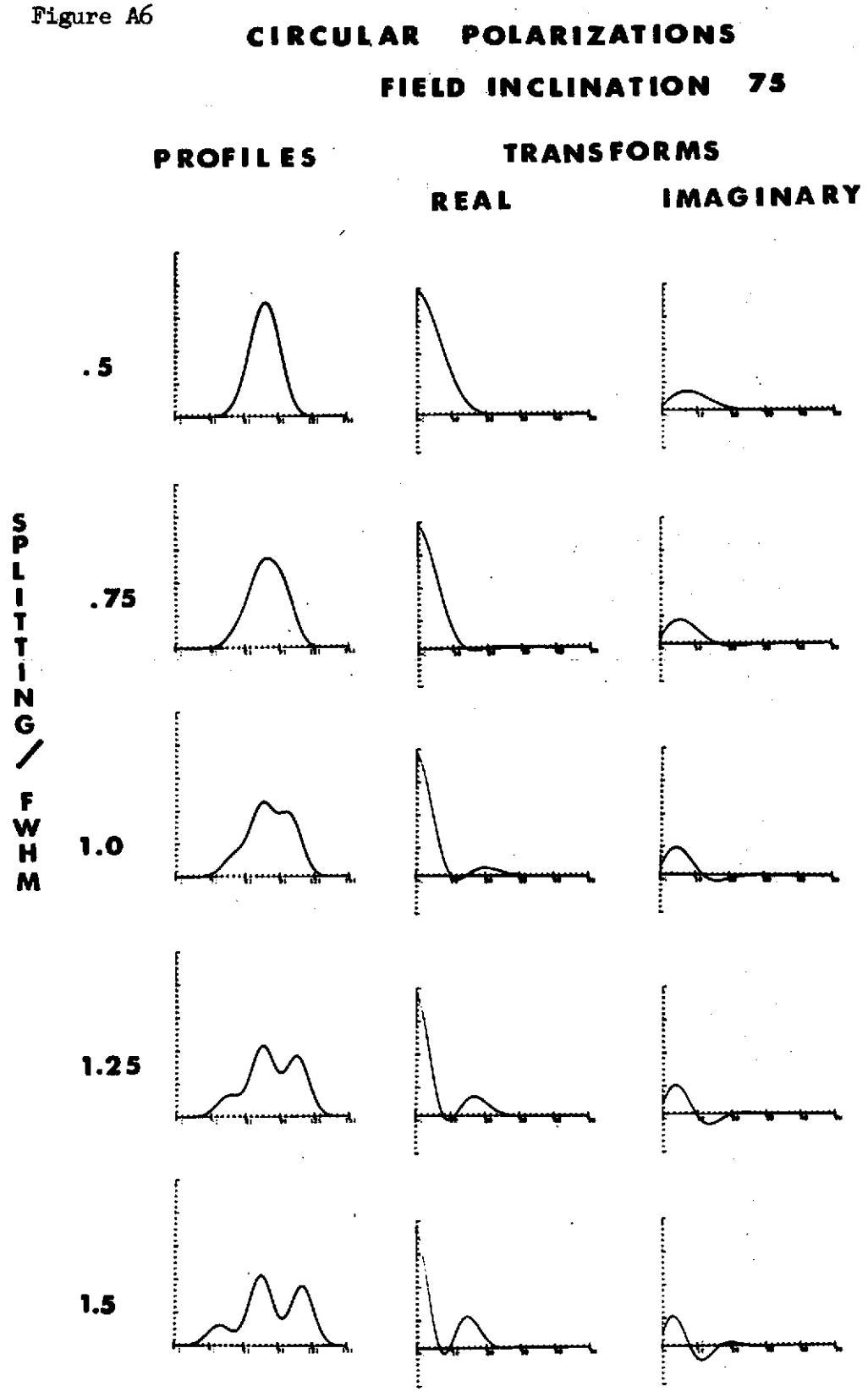
CIRCULAR POLARIZATIONS
FIELD INCLINATION 75
PROFILES
TRANSFORMS
REAL
IMAGINARY
SPLITTING / FWHM
.5
.75
1.0
1.25
1.5

APPENDIX II

Shown in Figures A7 through A15 are plots of Gaussian Zeeman profiles in pairs of orthogonal linear polarizations and the fourier transforms of the sum and differences of the pairs. The profiles and their transforms are organized differently from the circular case and a smaller fraction of the possible angular and splitting combinations are shown. Included are inclinations from the vertical from 30 to 90° in 30° steps, orientations with respect to the azimuthal projection of the field from 45° to 90° in 15° steps at three splitting to FWHM ratios. Each figure represents a single inclination from the vertical and a single splitting to FWHM ratio. The first two columns contain the profile at ± 45° to the azimuthal projection of the field. In the third column of the first row is the transform of the sum profile. The difference profile is zero and is not shown. Further since the sum profile is the same for all azimuthal orientations it is only shown in row one. All successive rows contain profiles in orthogonal polarizations at the indicated angles to the azimuthal projection of the field and the fourier transform of the difference profile.

Figure A7

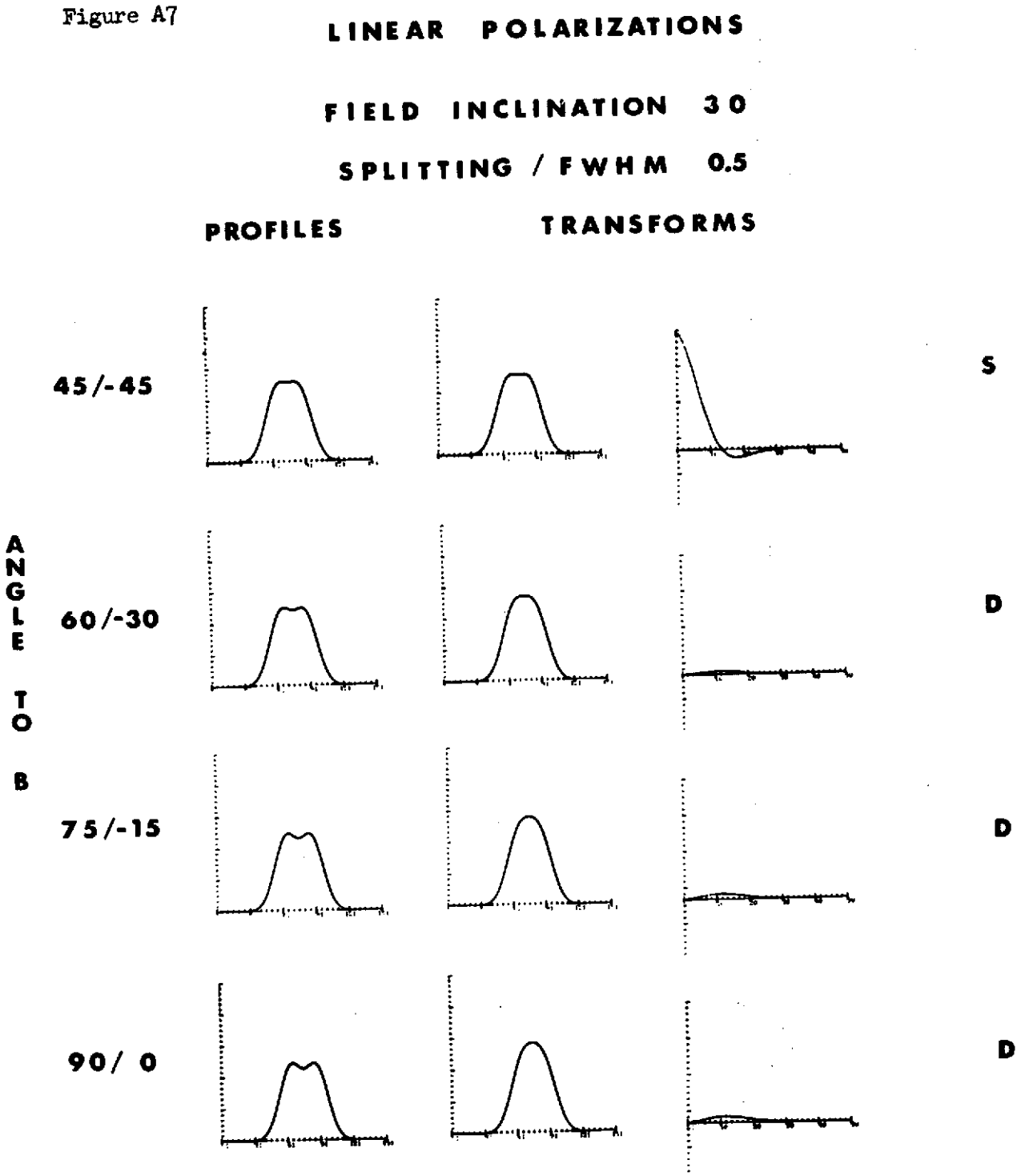
LINEAR POLARIZATIONS
FIELD INCLINATION 30
SPLITTING / FWHM 0.5
PROFILES
TRANSFORMS
ANGLE TO B
45/-45
60/-30
75/-15
90/ 0
S
D
D
D

Figure A8

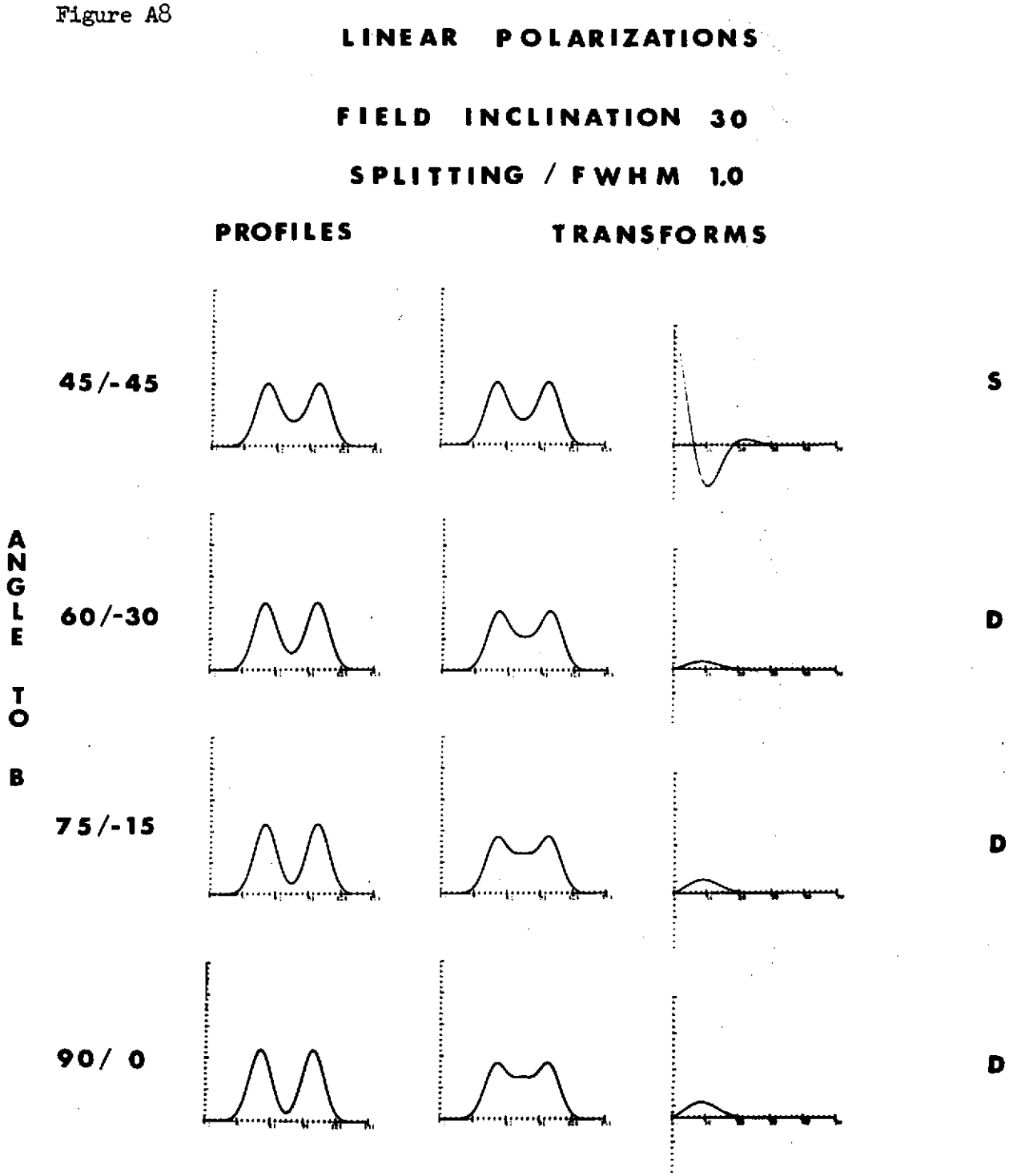
LINEAR POLARIZATIONS
FIELD INCLINATION 30
SPLITTING / FWHM 1.0
PROFILES
TRANSFORMS
ANGLE TO B
45/-45
60/-30
75/-15
90/ 0
S
D
D
D

Figure A9

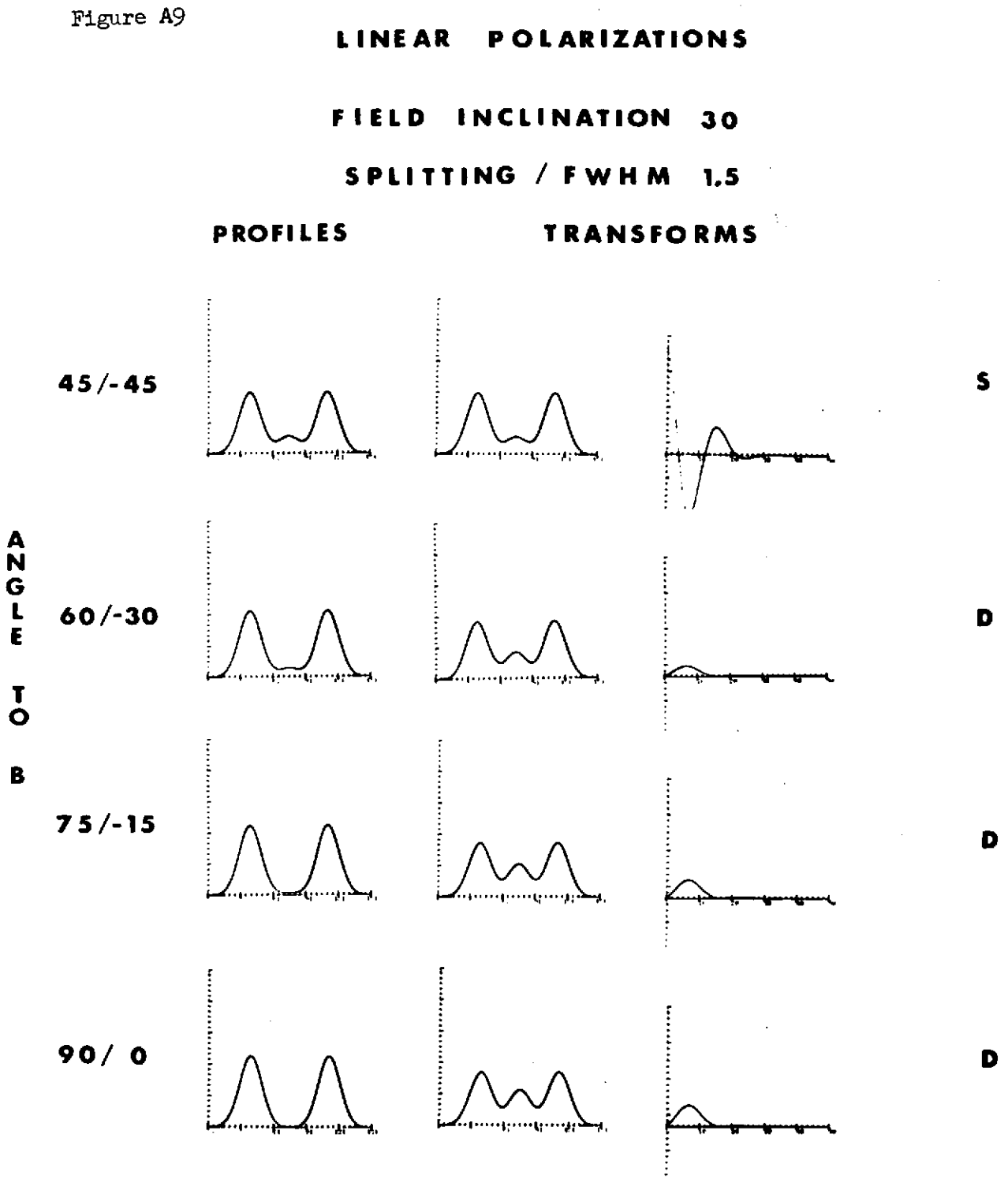
LINEAR POLARIZATIONS
FIELD INCLINATION 30
SPLITTING / FWHM 1.5
PROFILES
TRANSFORMS
ANGLE TO B
45/-45
60/-30
75/-15
90/ 0
S
D
D
D

Figure A10

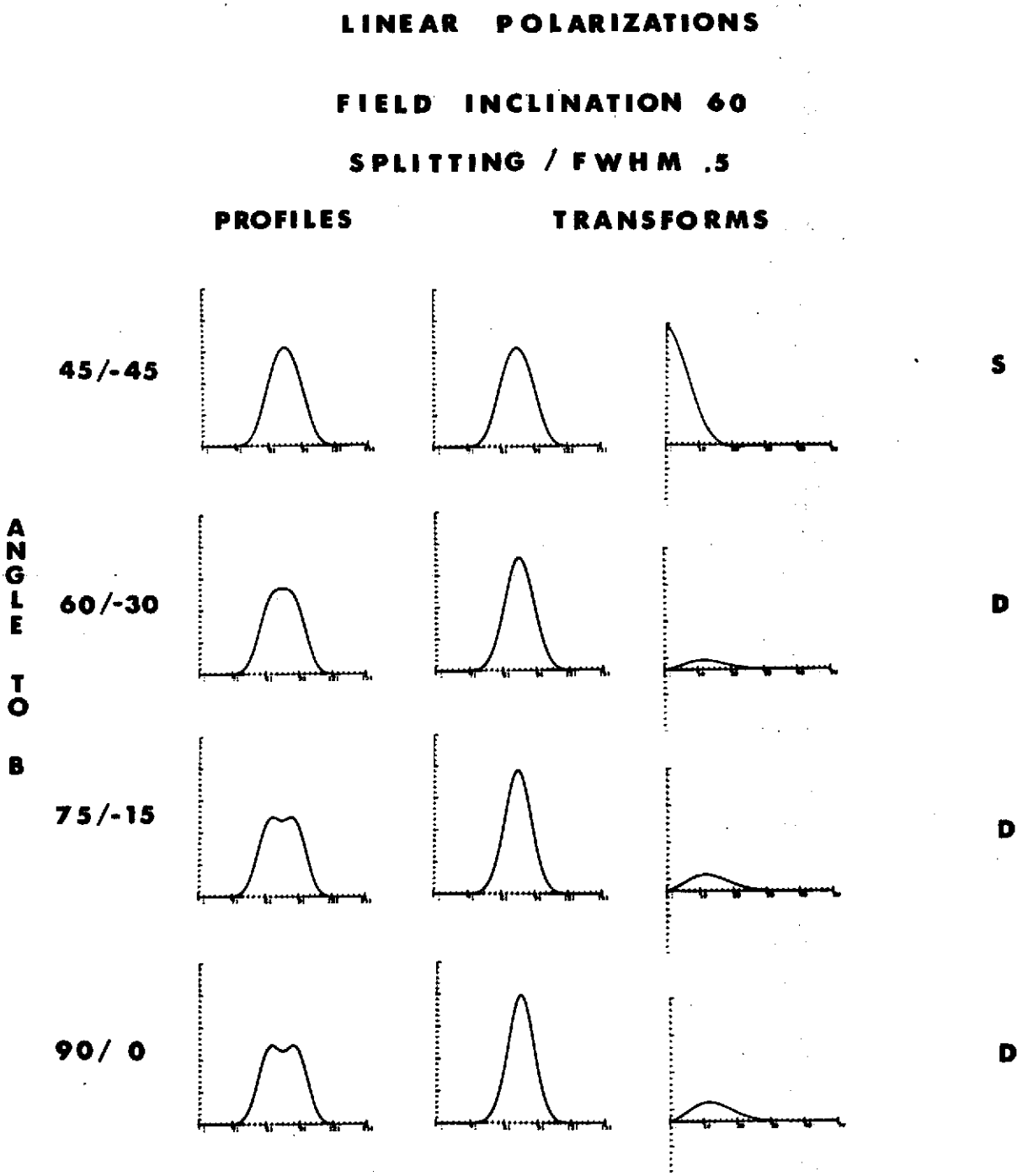
LINEAR POLARIZATIONS
FIELD INCLINATION 60
SPLITTING / FWHM .5
PROFILES
TRANSFORMS
ANGLE TO B
45/-45
60/-30
75/-15
90/ 0
S
D
D
D

Figure All

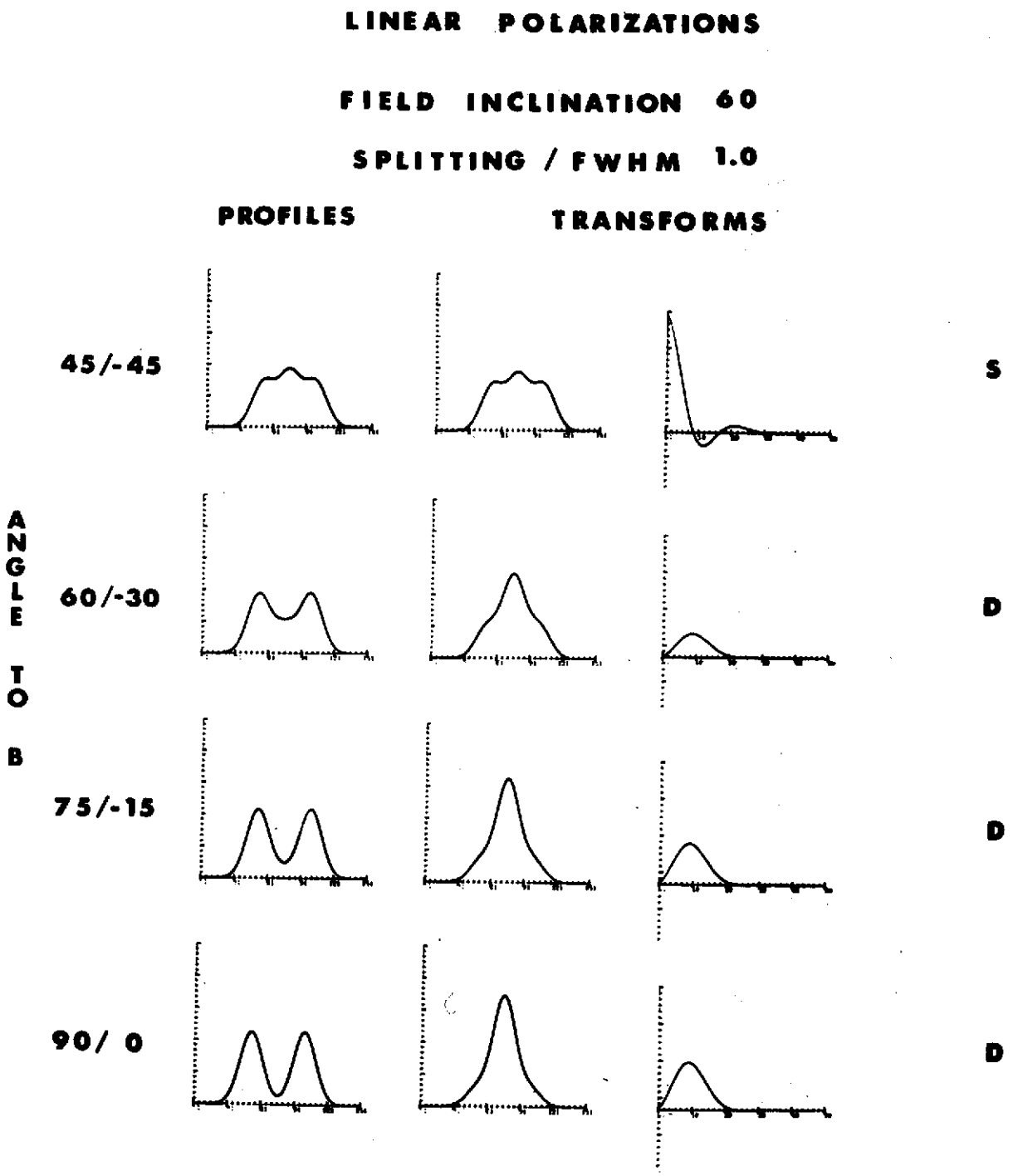
LINEAR POLARIZATIONS
FIELD INCLINATION 60
SPLITTING / FWHM 1.0
PROFILES
TRANSFORMS
ANGLE TO B
45/-45
60/-30
75/-15
90/ 0
S
D
D
D

Figure A12

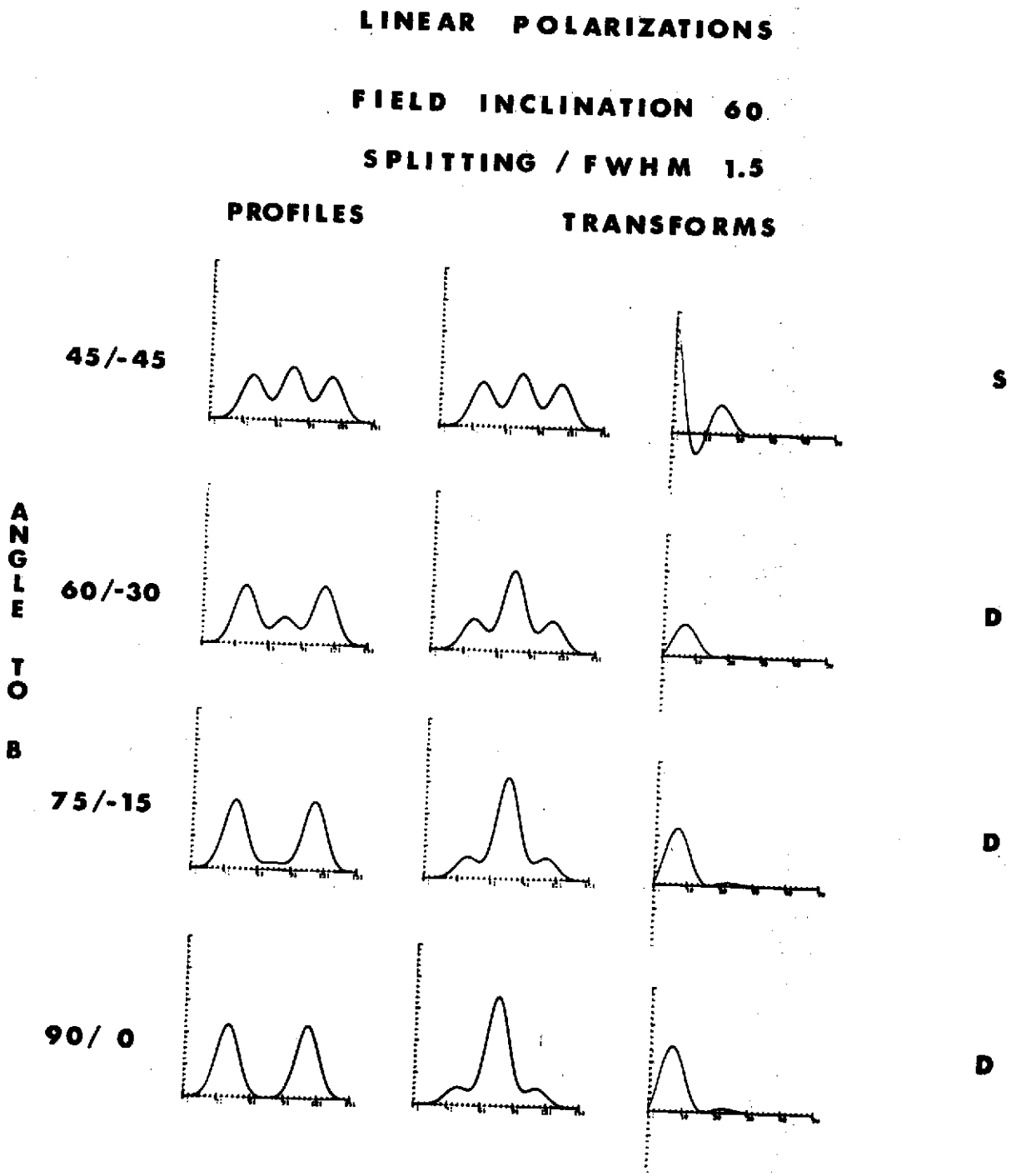
LINEAR POLARIZATIONS
FIELD INCLINATION 60
SPLITTING / FWHM 1.5
PROFILES
TRANSFORMS
ANGLE TO B
45/-45
60/-30
75/-15
90/ 0
S
D
D
D

Figure A13

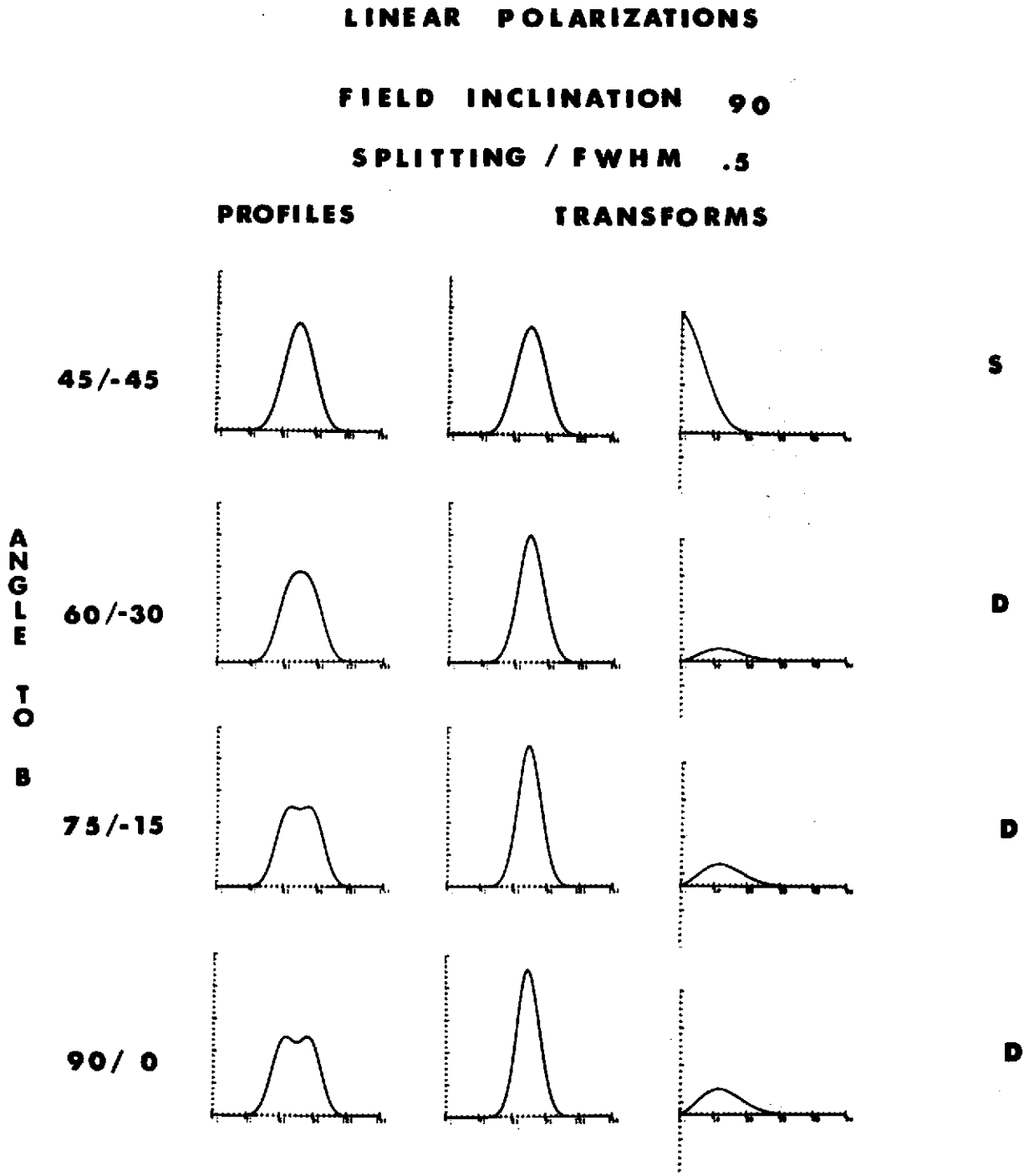
LINEAR POLARIZATIONS
FIELD INCLINATION 90
SPLITTING / FWHM .5
PROFILES
TRANSFORMS
ANGLE TO B
45/-45
60/-30
75/-15
90/ 0
S
D
D
D

Figure A14

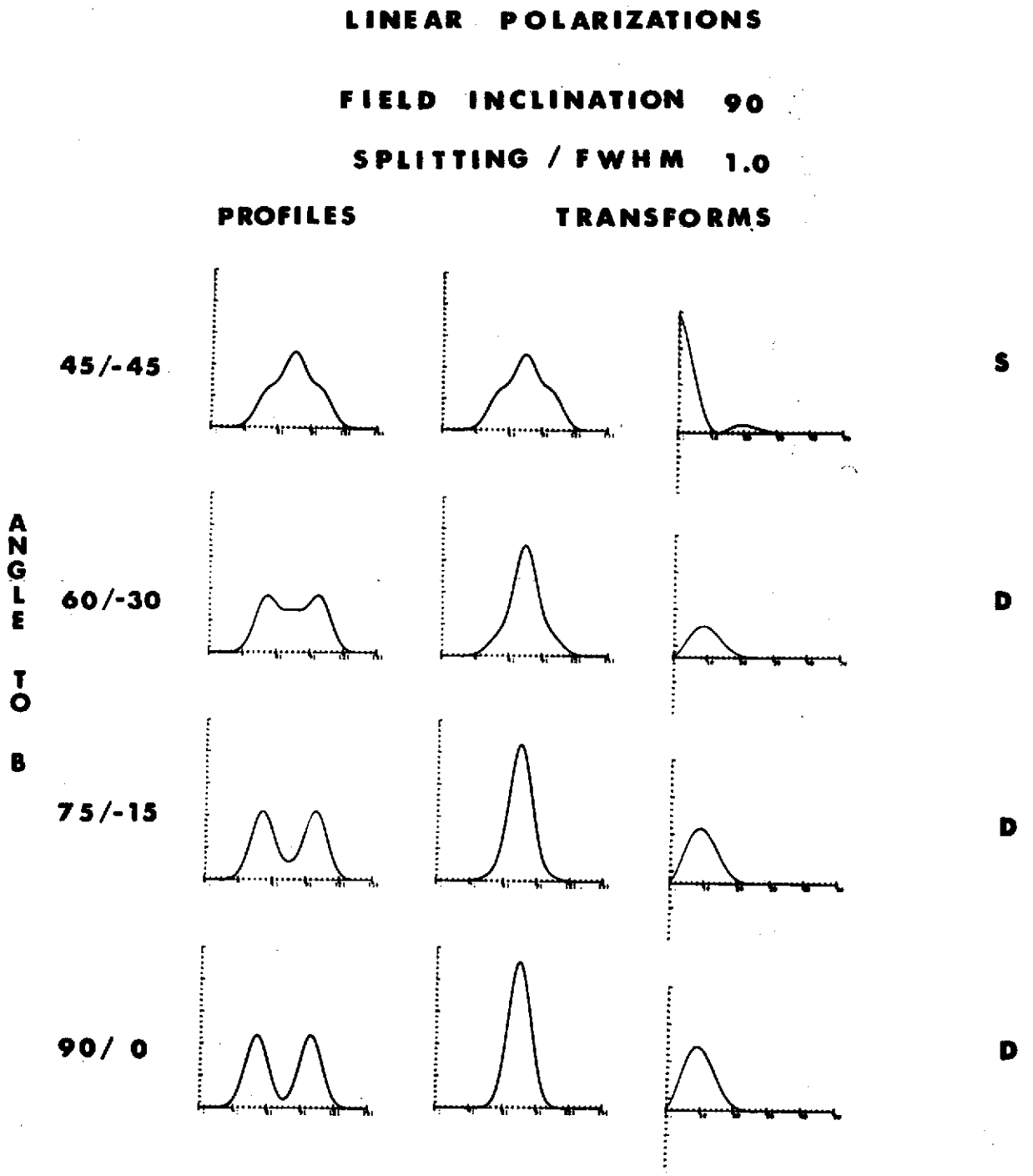
LINEAR POLARIZATIONS
FIELD INCLINATION 90
SPLITTING / FWHM 1.0
PROFILES
TRANSFORMS
ANGLE TO B
45/-45
60/-30
75/-15
90/ 0
S
D
D
D

Figure A15

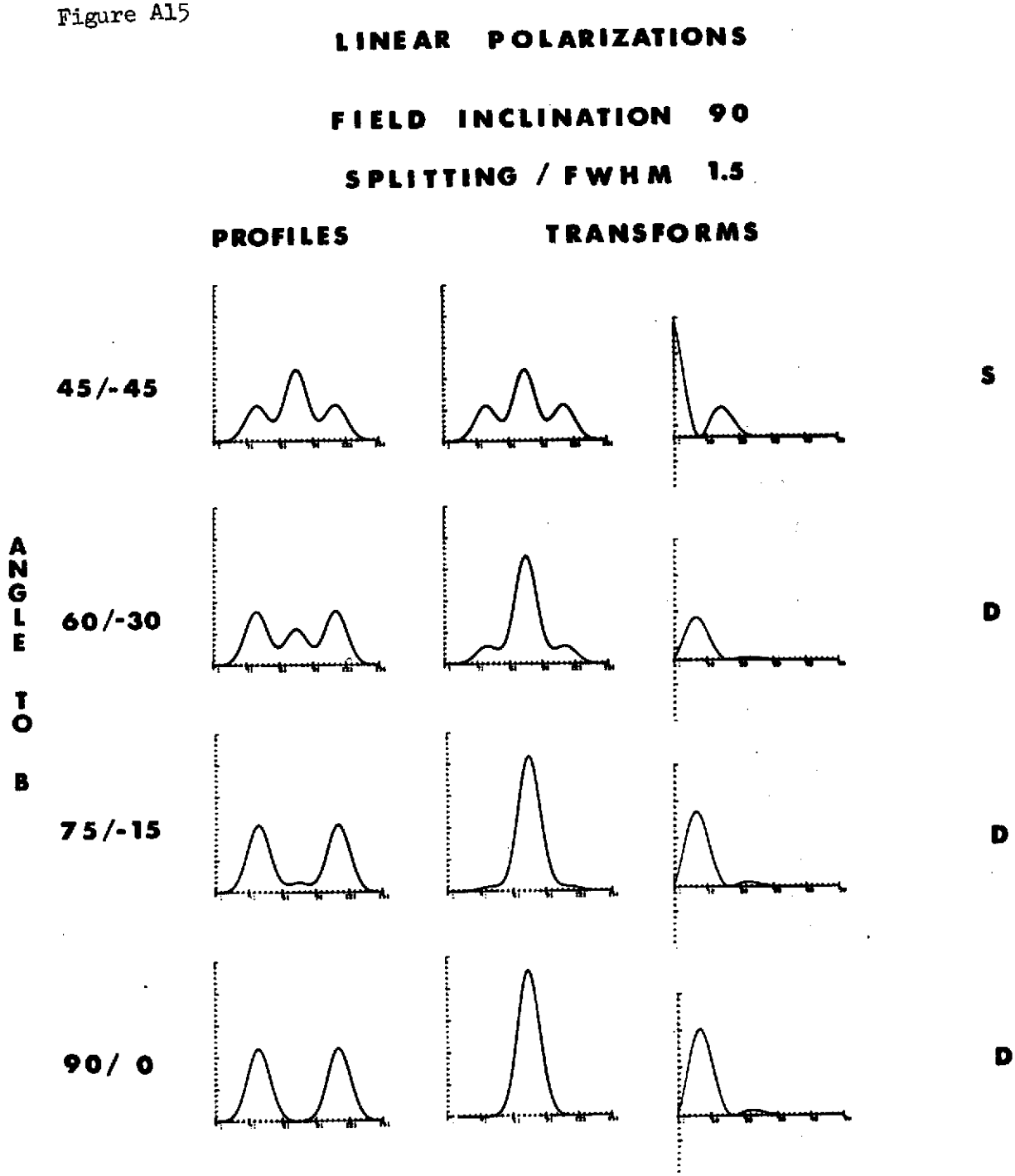
LINEAR POLARIZATIONS
FIELD INCLINATION 90
SPLITTING / FWHM 1.5
PROFILES
TRANSFORMS
ANGLE TO B
45/-45
60/-30
75/-15
90/ 0
S
D
D
D

C. CONTOUR MAPS OF A HIGH GRADIENT REGION

In the first paper on the Spectra-Spectroheliograph a sequence of original data was shown that apparently exhibited field reversal at a field strength of over 2000 gauss. In the course of all our observations this region presented the most complex magnetic structure. It was therefore chosen as the final test for the data reduction procedures.

Shown in Figures 8a and b are contour maps of the magnetic field strength ($|B|$), and the continuum intensity for the high gradient region. Corresponding points in 8a and b as well as 9a, b, and c, represent identical points on the surface of the sun. The field strength is shown in hundreds of gauss. The continuum intensity is in arbitrary units; however, lower numbers indicate lower intensities. The regions with intensities below 30 are umbral. Figures 9a, b, and c show contour maps of the longitudinal component of the field ($B \cos \gamma$), the inclination of the field (γ), and the line of sight velocity (V). The longitudinal component of the field is given in hundreds of gauss. The inclination of the field is given in degrees from the vertical. The velocity is in kilometer per second, positive downward.

Comparison of Figures 8a and 9a shows that the maximal field strength occurs where the longitudinal field is zero. For convenience the contour of zero longitudinal field is shown on the field strength map (8a) and is marked by zeros at the outside of the map boundaries. It is clear from 8a that there exist gradients of the order of 6000 gauss/arc second in the magnitude of field in the neighborhood of the zero longitudinal field contour. The maximum gradient in the longitudinal component of the field is approximately 700 gauss/arc second.

Comparison of Figures 9a and 9b shows that, at least for this region, the contours of the longitudinal field inside the spot are dominated by the inclination of the field. Figure 9c indicates that the velocity toward the surface apparently increases as the field inclination becomes more vertical.

The data reduction for the contour maps was performed completely automatically. The film was traced using the roster features of program TRACE in less than five minutes. The data on the computer was reorganized under a program called PASS2 (see Section 2) in a running time of 8 minutes. Then the data for the maps were created by PASS3 in slightly under 20 minutes.

FIGURE CAPTIONS

Figure 8. Contour map of Sunspot High Gradient Region. a - Magnitude of the field in hundreds of gauss. b - Continuum intensity in arbitrary units.

Figure 9. Contour map of Sunspot High Gradient Region. a - Longitudinal component of the field (B cos γ). b - Inclination of field to line of sight (γ). c - Line of sight velocity (positive downward).

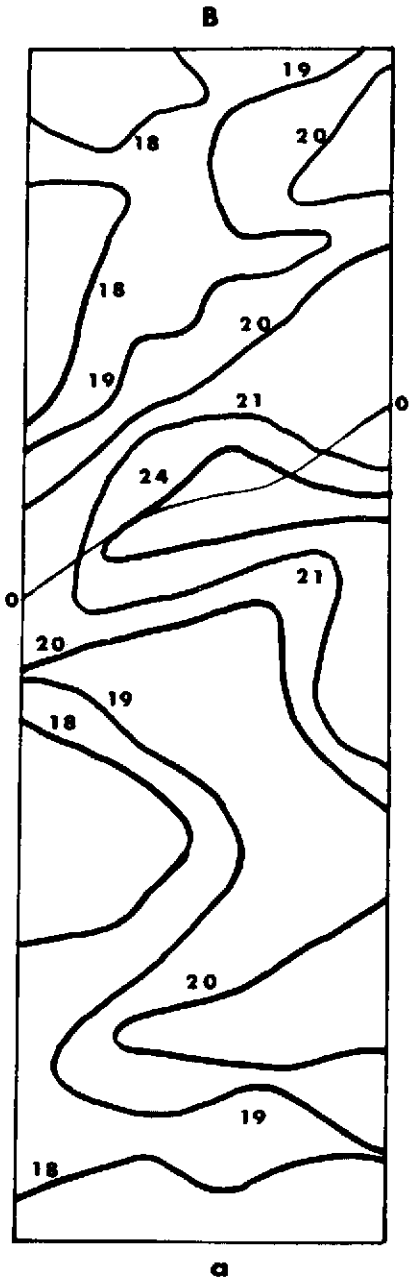

Figure 8a

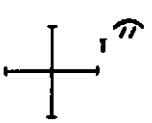

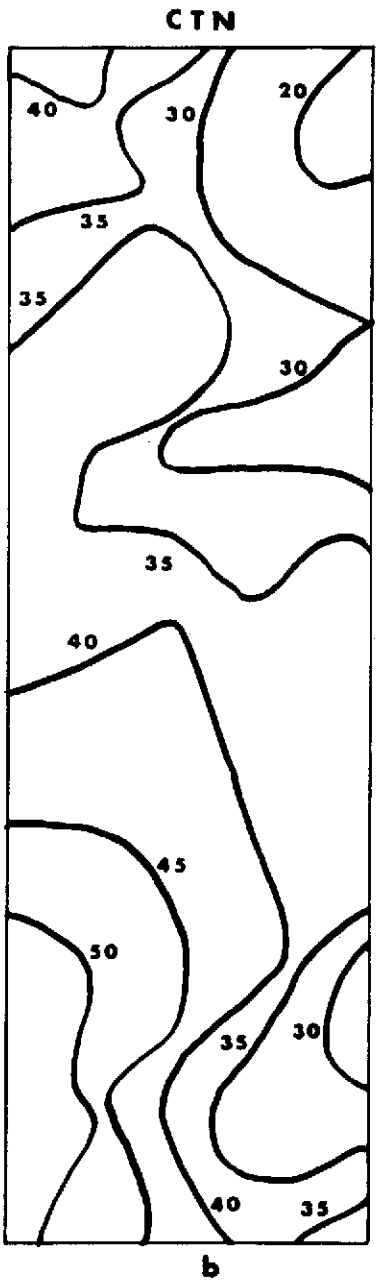

Figure 8b

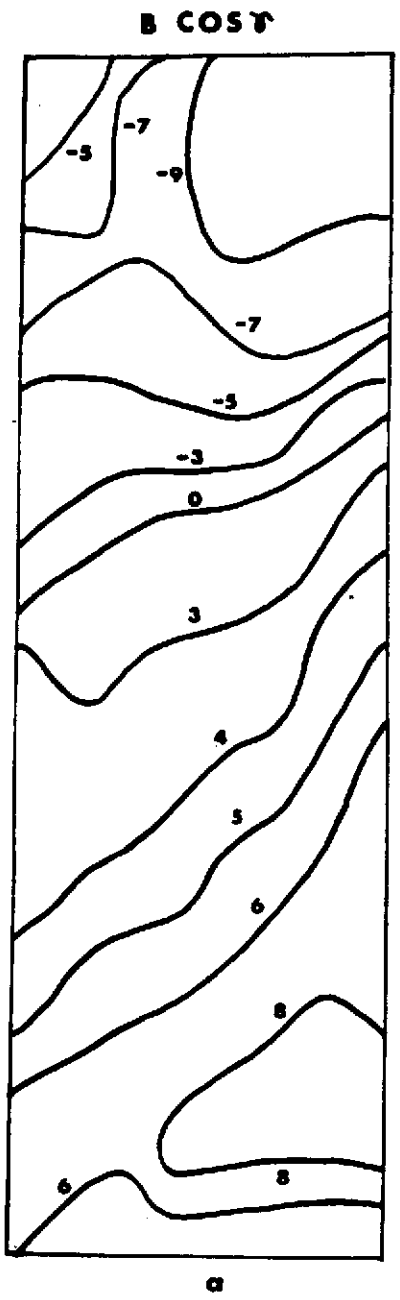

Figure 9a

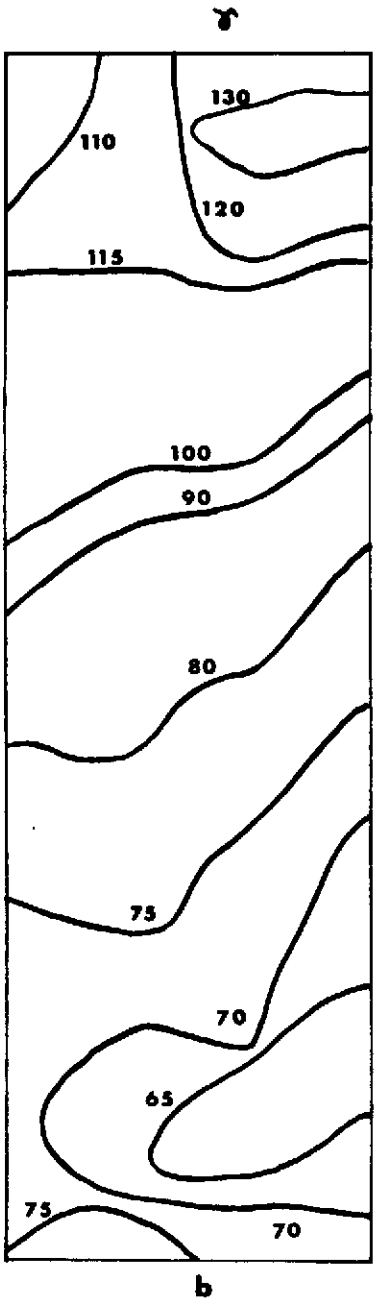

Figure 9b

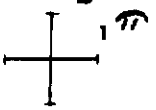

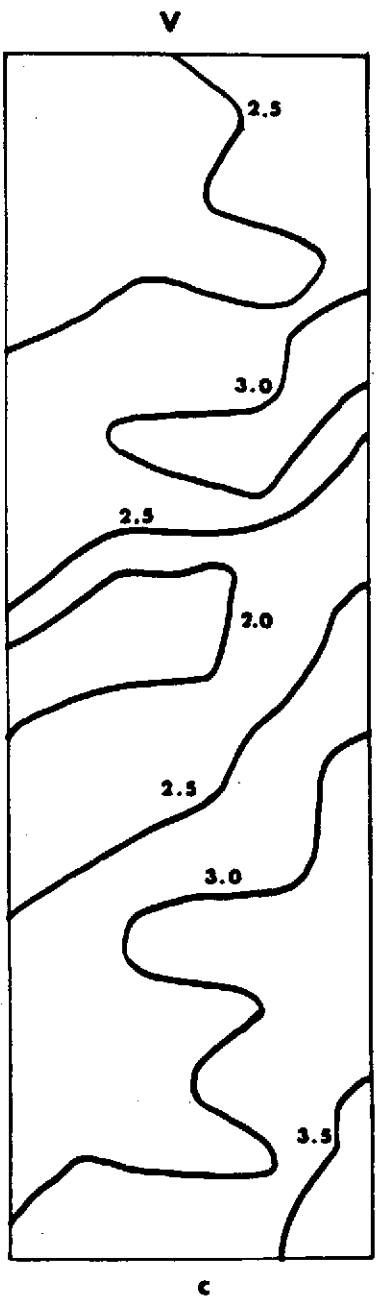

Figure 9c

D. DATA REDUCTION PROCESS

As an illustrative example, let us consider the reduction of the Hα spectra of the flare of 5 September 1973 as recorded by Lockheed's multi-slit spectrograph (MSS). This event was seen and studied by Skylab. A sample of the MSS data is shown in Figure 10. The MSS differs from a conventional spectrograph in that many entrance slits are placed at the solar image. A 7 Angstrom blocking filter centered on Hα is introduced into the beam to prevent the spectra from the several slits from overlapping.

The spectra were first digitized with the PDS microdensitometer. (The densitometer, the associated PDP-11 computer, and the control software which facilitates the use of the densitometer, are described in detail elsewhere in this report.) A total of 43 frames (taken at 15 second intervals) were traced. This covered the period from just before the onset of the flare to well into the declining phase. On each frame, 70 positions along the slit were traced, each separated by about one arc second. A calibrated step wedge was also traced. The data were in the computer's disk memory.

The processing of the numerical data proceeds in three steps. First, the raw digital data are converted to relative intensity values, using the step wedge results and the known characteristic curve of the film. Next, the profile of the 7 Å blocking filter was divided out, thereby recreating the original solar spectral profile. Finally, the results are displayed and compared in several ways.

One obvious display is the comparison of a profile to the pre-flare profile at the same location. This can be done both for successive positions along the slit and for successive times at a given slit location. An example is shown in Figure 11. The drawings are made with a computer-controlled CRT.

We have found that a particularly useful display is produced by stacking the profiles diagonally one behind the other. This gives a perspective view of the flare spectrum along the slit. Examples from selected frames are shown in Figure 12. Moreover, when these perspective views are projected cinemagraphically, the spectral dynamics of the entire event become clear. This display is included in the 16 mm film which is appended to this report.

FIGURE CAPTIONS

Figure 10. Multislit spectrograph in Hα for the flare of 5 September 1973.

Figure 11. Flare profile (solid line) compared to the preflare profile (dotted line).

Figure 12. Perspective view of the flare spectrum along the slit. Each frame shows the spatial distribution.

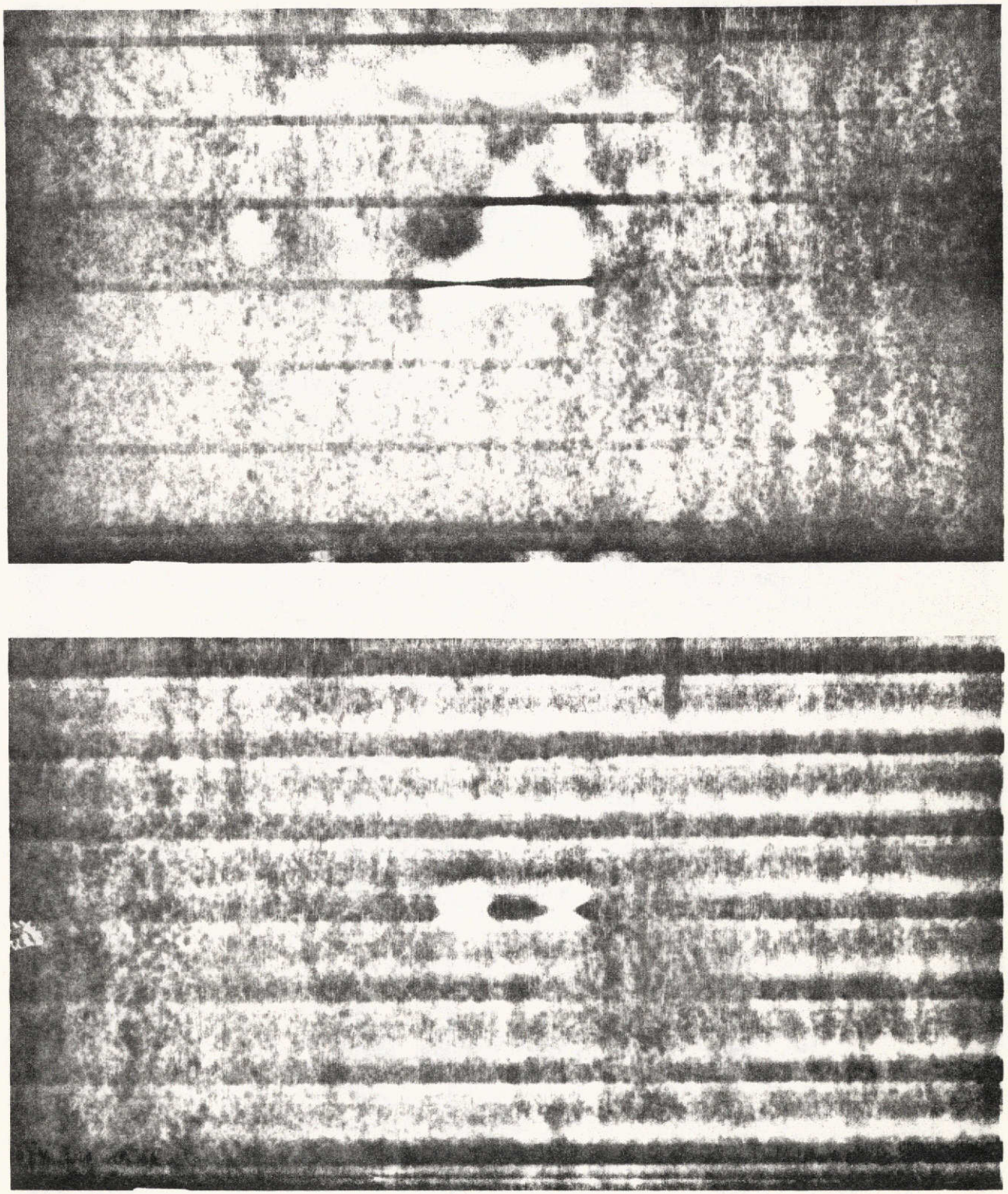

Figure 10

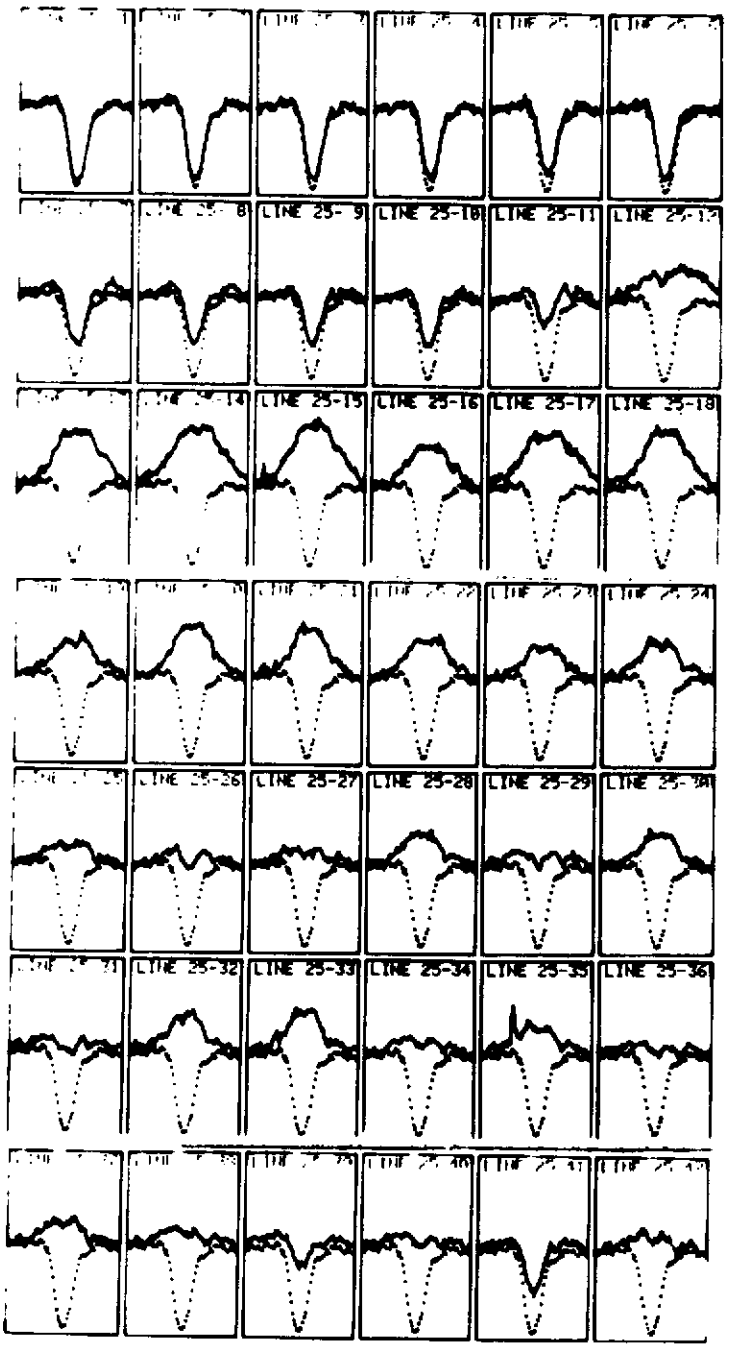
LINE 25- 9
LINE 25-10
LINE 25-11
LINE 25-15
LINE 25-16
LINE 25-17
LINE 25-18
LINE 25-27
LINE 25-28
LINE 25-29
LINE 25-32
LINE 25-33
LINE 25-34
LINE 25-35
LINE 25-36

Figure 11

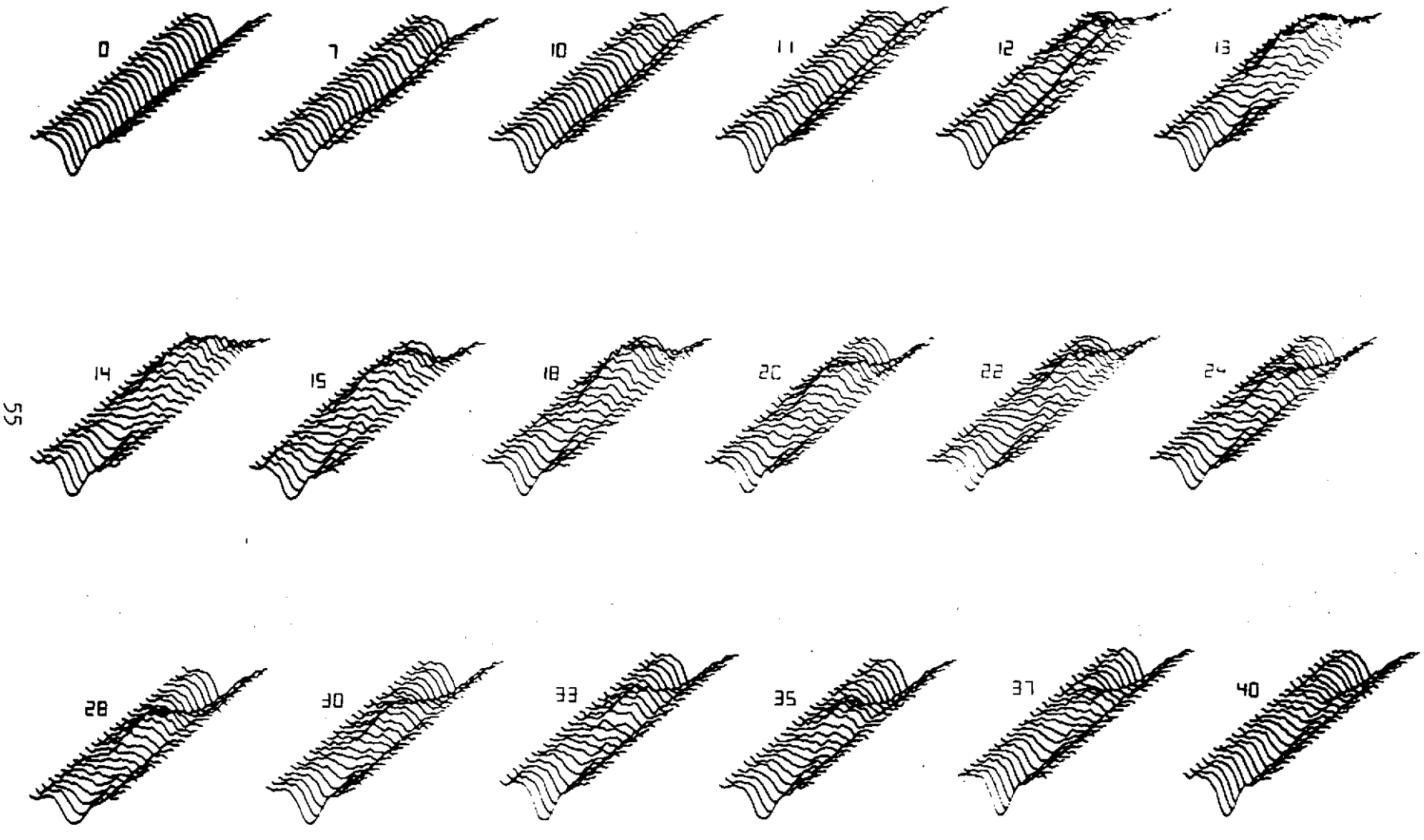

Figure 12

E. THE FLARE OF 5 SEPTEMBER 1973 - A FILM

The accompanying 16 mm film shows the solar flare of 5 September 1973 (a Skylab event) as recorded and measured by the Lockheed Solar Observatory. The film consists of six sequences, each covering approximately the same period of time, but each showing the event in a different way. Only when all of these aspects, plus others not detected at Lockheed, are taken into account can a coherent picture of the flare process be assembled.

Sequence 1. This shows a direct view of the flare as seen through a filter centered on Hα (the Balmer-α line of neutral hydrogen at 6563 Å). The pictures were taken by the slit monitor camera of the multi-slit spectrograph. The vertical black lines are the entrance slits of the spectrograph.

Sequence 2. This shows a series of Hα spectra as recorded by the multi-slit spectrograph. A 7 Å filter, centered on Hα is placed in the optical path. Thus, each entrance slit produces a segment of spectrum about 7 Å wide. The slits are sufficiently separated that there is only a small overlap between adjacent segments. The vertical dark lines seen in the pictures are each the core of the Hα line coming from a single slit. As the sequence progresses, the bright flare can be seen in emission (bright) in the center of Hα. The rapidly moving surges appear in absorption (dark) and are Doppler-shifted away from the core of the line. Blue (shorter wavelength) is to left, red to the right.

Sequence 3. The flare is seen through a narrow filter centered 1.2 Å to the blue (short wavelength) side of the center of Hα. Thus, features which are rising from the sun and are thereby Doppler-shifted toward the blue will appear prominently.

Sequence 4. This is similar to Sequence 3, except that the filter sits on the red side of Hα, so that falling features appear prominently.

Sequence 5. This is a repeat of parts of sequences 1 (slit monitor) and 2 (multi-slit spectra). The arrow indicates the slit along which the flare spectrum has been digitized. In the multi-slit spectra sequence, note that the bright flare emission occurs at two slightly separated positions along the slit.

Sequence 6. This shows, in animation, the spectral dynamics of the flare. The data were digitized with the PDS microdensitometer, scanning perpendicular to the slit. After reduction, the individual traces along the slit were drawn on a CRT stacked one "behind" the other, so as to give a perspective view of the spectral intensity along the slit. The sequence is divided into two parts, each taken from one of the two bright emission features indicated in Sequence 5. Note that the center of the line goes into smooth emission in the first part, while a "self-reversal" absorption profile persists at line center in the second part.